A Computational Investigation of Canted Side-by-side Rotors In Ground Effect

Richard Healy PhD Candidate
Farhan Gandhi Redfern Professor
Center for Mobility with Vertical Lift (MOVE), Rensselaer Polytechnic Institute, New York, USA

ABSTRACT

This study investigates the interactional aerodynamics of canted side-by-side rotors hovering in ground effect. The 5.5 ft diameter 3-bladed fixed-pitched rotors are simulated using CFD at a targeted 5 lb/ft^2 disk loading. Simulations are performed using the commercial Navier Stokes solver AcuSolve® with a delayed detached eddy simulation (DDES) model. Side-by-side rotors are simulated at a height above the ground equal to one rotor radius (z/R = 1.0) and with 2.5R hub-hub spacing. In addition to an uncanted case, side-by-side rotors are simulated in ground effect (IGE) with 10° differential lateral cant, 10° inwards cant, and 10° outwards cant. Between the uncanted side-by-side rotors IGE, a highly turbulent mixing region is identified where the wakes of each rotor collide and fountain up. As blades traverse the highly turbulent flow, strong vibratory loading is induced and a thrust loss is observed over the outboard blade sections. The associated unsteady vertical loading for uncanted, laterally canted, and canted outwards rotors is similar, ranging from 10% - 16% peak-to-peak whereas canted inwards rotors show increased vibratory loading at 22% peak-to-peak. Integrated thrust for uncanted rotors IGE is 4.3% more than if out of ground effect (OGE), though when laterally canted or canted outwards, thrust generation is reduced to within 1% of isolated OGE rotors. Canted inwards rotors produce even less thrust, generating 15.2% less thrust than isolated OGE rotors. Overall, canting side-by-side rotors IGE incurs thrust production and vibration penalties. If canting is required for improved control authority, laterally canted rotors generate the most thrust while canted outwards rotors generate the least vibratory loading.

INTRODUCTION

Over the last several years there has been a significant interest in large multi-rotor eVTOL aircraft for Urban Air Mobility. One of the challenges associated with the modeling, simulation and performance prediction of these aircraft is the complex interactional aerodynamic flow fields of multiple rotors operating in close proximity. Several recent studies have used high-fidelity computations to represent these flows (see for e.g., Refs. 1–12), resulting in valuable physical insights as well as an understanding of beneficial geometries/configurations. It should be noted though, that most of the above multi-rotor eVTOL interactional aerodynamic studies have all been conducted out of ground effect (OGE). During take-off and landing operations however, these multicopters will be close to the ground, and rotor-rotor-ground aerodynamic interactions can be expected to strongly influence the rotor performance and loads.

Although the understanding of rotors in ground effect (IGE) is not new, the majority of prior studies in this area have focused on conventional single main rotor aircraft, or an isolated rotor in proximity of the ground. Early experiments by Fradenburgh (Ref. 13) identified performance improvements for rotors operating near the ground, and characterized how the wake moves radially outward after impacting the ground. Fradenburgh also identified flow inside the rotor wake moving upwards, towards the rotor disk. Other experiments have consistently reported improved rotor performance when operating within one rotor diameter of the ground, and have been used to develop empirical models for rotors IGE (Refs. 14–17). Experimental studies of rotors in forward flight ground effect have also revealed flow recirculation at low advance ratios leading to unsteadiness and an increase in power (Refs. 18–21).

Presented at the Vertical Flight Society's 79th Annual Forum & Technology Display, West Palm Beach, Florida, USA, May 16–18, 2023.

In recent studies, combinations of computational and experimental methods have been used to further understand ground effect aerodynamics. Several works have used free-vortex wake models to predict the radial wake spread of hovering rotors IGE, as well as the recirculating flow of forward-flight rotors IGE (Refs. 22–26). Experiments and computational fluid dynamics (CFD) simulations by Wadcock et al. have also shown significant flow unsteadiness and upwash through the middle of the rotor disk due to ground effect on a UH-60 (Ref. 27). Similar findings have been reported by Kutz et al. who observed a 21% increase in thrust, as well as load oscillations when a Hughes 300C was simulated near the ground using CFD (Ref. 28). Fluctuations in power have also been reported by Brown and Whitehouse who describe unsteadiness due to flow fountaining through the hub region in hover, as well as flow being reingested into the rotor during low speed forward flight (Ref. 29). At smaller scales, Lakshminarayan et al. simulated a micro-scale rotor IGE and observed a thrust increase given constant power relative to when operating out of ground effect (Ref. 30). Flow unsteadiness was also observed below the rotor, which grew stronger as the rotor was brought closer to the ground.

While much of the existing ground effect literature focuses on single main rotor helicopters, there exists a body of work providing insights into some dual-rotor configurations, namely CH-47 tandem rotors IGE (Refs. 31–33) as well as V-22 and XV-15 tilt rotors (Refs. 34–37). The focus of tandem rotor configurations has mostly been related to the impact of rotor overlap on outwash, however most large eVTOL vehicles employ non-overlapped rotors for thrust generation and control. Tiltrotors in hover provide more relevant insights into multi-rotor operation IGE with ground effect-like conditions being observed on portions of the rotor disks positioned over the wings. Rotor outwash over the wings has been shown to fountain up, over the centerline of the vehicle and be reingested into the rotors, leading to reduced rotor performance (Refs. 34–37). The unique aerodynamics of these multiple close proximity rotors has prompted investigations into other multi-rotor configurations IGE. Actuator disk CFD simulations on a quad-tiltrotor by Gupta and Baeder showed highly complex flows between rotors when in close proximity to a ground plane (Ref. 38). Other experiments on a quad-tiltrotor by Radhakrishnan and Schmitz attributed performance improvements IGE to upwash induced by colliding rotor wakes impinging on the underside of the fuselage (Refs. 39–42). Multi-rotor interactions IGE have also been reported by Miesner et al. who simulated the eighteen rotor Volocopter 2x using CFD, and saw load fluctuations strengthen as the rotors were brought closer to the ground (Ref. 11). Fluctuations were linked to mixing vortex structures between rotors which grew stronger close to the ground. Larger vortex structures were observed between rotors that were spaced farther apart. Unsteady flow between rotors has also been reported by Healy et al. who simulated side-by-side rotors in ground effect using CFD and observed inter-rotor thrust deficits negating the nominal ground effect benefits (Ref. 43).

Whereas the studies above have simulated multi-rotor configurations with uncanted rotors, many modern eVTOL designs are incorporating canted rotors where the axis of rotation is inclined from the vertical (Fig. 1) in an effort to realize benefits that include improved yaw authority (Refs. 44–47). Rotor canting can significantly improve yaw control authority by using a component of the thrust generated by the rotors to produce aircraft yaw moments (Refs. 47, 48). However, the effect of rotor canting on aerodynamic performance, especially on the interactional aerodynamics for multirotor assemblies, is largely unknown. Previous work has identified how cant affects rotor-rotor interactional aerodynamics in forward-flight OGE (Ref. 4). Additionally, some works have investigated the performance of canted rotors IGE. Simulations of a tilted ducted rotor IGE using actuator-disk CFD by Hosseini, Ramirez-Serrano and Martinuzzi showed only a very slight thrust reduction as the ducted rotor angle was increased IGE (Ref. 49). Other experiments by Tritschler, Milluzzo and Holder showed increased power requirements for a canted IGE rotor over an uncanted one (Ref. 50). However, these studies and others are are concerned with single rotor operation IGE. The understanding of how multiple canted rotors perform IGE is still limited and is particularly important considering the utility of cant on multi-rotor aircraft.

The present work uses high fidelity blade resolved CFD to extend the work in Ref. 43 and investigates the aerodynamics of multiple close proximity canted rotors in ground effect. In particular, comparisons are made between canted and uncanted side-by-side rotors operating near the ground. The relative direction of rotor cant is varied, and the aerodynamic interaction between rotors and the ground is investigated. Physical explanations of differences in rotor performance between cases is also provided.

Figure 1: Laterally canted rotors on the Boeing PAV. Reprinted with permission from the Vertical Flight Society (Ref. 51)

ANALYSIS

Three single rotor and four side-by-side rotor cases are simulated using CFD. Single rotors are simulated in hover OGE and at one rotor radius above the ground (z/R = 1.0) with and without cant. For the canted rotor, the axis of rotation is tilted 10° about the ψ = 90° - 270° line with the part of the disk at ψ = 0° angled down. Side-by-side rotors are also simulated in hover IGE at z/R = 1.0 uncanted, and with three cant types: differential lateral cant, differential longitudinal cant inwards and differential longitudinal cant outwards (shown in Fig. 2). For differential lateral cant, each rotor is rotated 10° about the axis connecting both rotor hubs. In particular, both rotors are angled with ψ = 90° oriented upwards. For longitudinal cant inward, the rotors are tilted 10° such that their thrust vectors point towards the other rotor. In the other direction, longitudinal cant outward is defined such that the rotors are each tilted 10° with their thrust vectors pointing away from the other rotor. For all side-by-side rotor cases, the left rotor spins clockwise, and the right spins counterclockwise with hub-hub spacing equal to 2.5 rotor radii.

The rotors used have a 5.5 ft diameter, with specifications detailed in Table 1, and are fitted with an idealized teardrop shaped hub to reduce (albeit not eliminate) the root wake and upwelling through the hub (Refs. 52, 53). The Rensselaer Multirotor Analysis Code (RMAC) (Ref. 54), based on blade element theory (BET) with 3x4 finite state Peters-He inflow representation is used to evaluate an appropriate root pitch and RPM for a target 5 lb/ft^2 disk loading in hover OGE. A 22° root pitch, and a rotational speed of 1600 revolutions per minute is found to provide low power and hover tip Mach number. A low tip Mach number is desired to avoid compressibility effects and reduce noise. Rotor RPM is held constant for all cases while comparing rotor thrust and torque in different configurations and conditions.

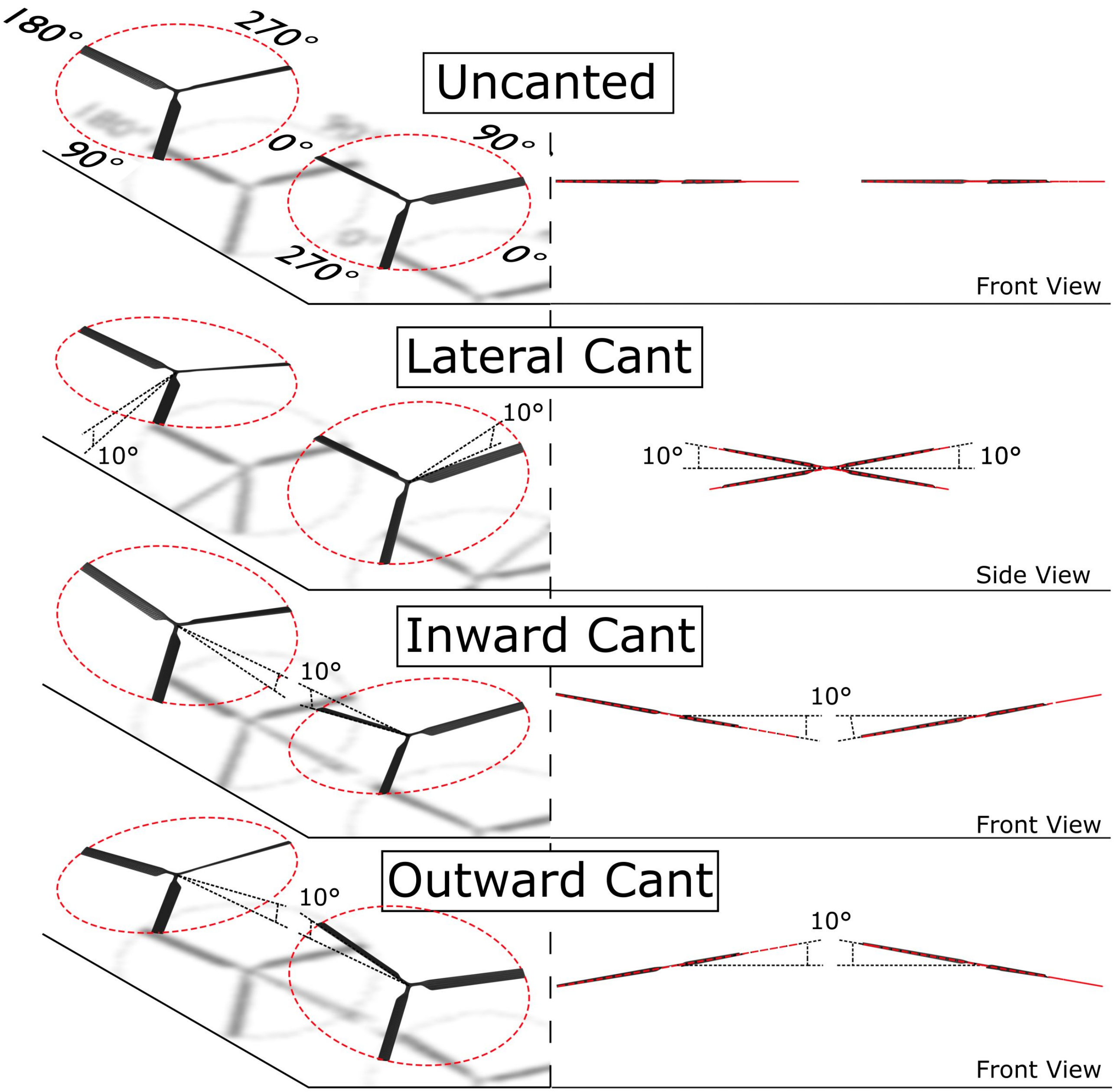

Figure 2: Isometric and side views of the four two rotor cases: uncanted, lateral cant, longitudinal cant in and longitudinal cant out

Table 1: Rotor Parameters

Parameter	Specification
Diameter	5.5 ft
Number of Blades	3
Solidity	0.076
Root Cutout	0.2R
Airfoil	NACA 23012
Twist	-10° / span
Planform	Rectangular
Chord	3.28 in
Root Pitch	22°
RPM	1600 RPM

All simulations are conducted using the commercial Navier-Stokes solver AcuSolve® which uses a stabilized 2nd-order upwind finite element method, and is validated for external aerodynamic flows (Refs. 55, 56). AcuSolve® simulation results for an SUI Endurance rotor in hover were previously shown to compare well against experiment in (Ref. 1) where thrust at two different rotor speeds in hover matched experiment within 3%. In addition to this OGE hover validation, AcuSolve® simulation of an IGE rotor has also been compared to experiment reported in (Ref. 14). The IGE thrust predicted by AcuSolve® is found to differ from experiment by 0.85%, with additional details presented in the appendix. For an uncanted 2-rotor unit, the computational domain is shown in Fig. 3. The nonrotating volume is a rectangular prism with sides at least 25 rotor radii away from the front rotor hub. The sides and top boundaries are set to outflow with backflow conditions enabled, which allows for flow in either direction across the boundary with zero pressure offset. The bottom surface is set to no-slip condition in a weak fashion with a log-law based wall function (Ref. 57). The weak boundary condition acts like a wall model (Ref. 58) without the impractical computational cost associated with resolving the boundary layer on the ground. No-slip wall condition (enforced strongly or weakly) has been found to capture viscous effects which are associated with predicting rotor performance IGE (Ref. 59). Around each rotor is a cylindrical rotating volume with radius 1.06 rotor radii and extending two chord lengths above and below the extents of the rotor hub. Each surface of the cylindrical rotating volumes has a sliding mesh interface which passes information to and from the non-rotating volume that comprises the remainder of the computational domain.

The computational domain is discretized using an entirely unstructured mesh comprised of tetrahedral elements. On each blade, the surface mesh is set to ensure 200 elements along the blade span and 200 elements around the airfoil contour, with refinement along the leading and trailing edges (0.14% chord first element height and 1.125 growth rate). The boundary layer in the wall-normal direction is highly resolved, with the first element height set to ensure a $y+ < 1$, which conforms to the requirements in Ref. 60 and is consistent with those used in Ref. 61. The boundary layer is grown until the last layer size is within 80% of the local off-body element size (43 layers total). A portion of the blade surface mesh and a clipped

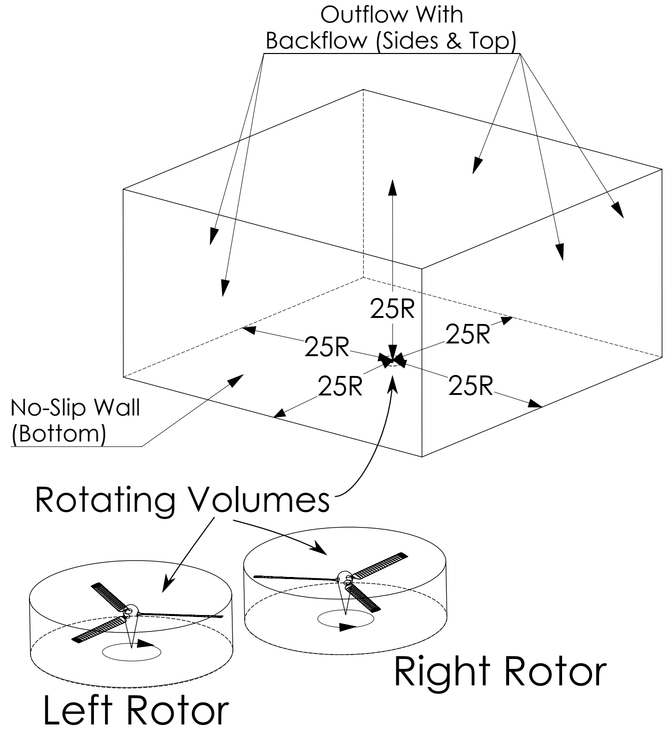

Figure 3: Diagram of the computational domain

slice of the boundary layer mesh is shown in Fig. 4. Around the rotors (0.75R above and below), a cylindrical wake refinement region (2.5R radius) is defined in which the element size is prescribed as 25% blade chord (shown for a single rotor in Fig. 5). Below the first refinement region is a second refinement region which is prescribed with elements 50% blade chord in size (Fig. 5). This refinement region extends radially from each rotor hub, extending 1.5R above the ground with 3.5R radius, and 0.25R above the ground with 10R radius. A third refinement region with 1.0 blade chord element size extends radially 10 rotor radii from each rotor hub and 3.25R above the ground (Fig. 5). All near-rotor refinement regions are set to remain aligned with the rotor thrust vector, meaning that for canted rotor cases, the refinements tilt with the rotor.

A boundary layer mesh is also grown off of the ground to capture the associated viscous effects. For this boundary layer, ensuring a $y+ < 1$ across the entire ground plane incurs substantial computational cost that can be avoided in this case through the use of wall modeling, which allows for $y+ < 100$ to be acceptable. At this grid scale, weakly enforcing no-slip conditions with log-law based wall models has been shown to capture the same mean-flow quantities as those produced by a fully-resolved boundary layer (Ref. 58). The use of wall modeling on the ground plane is estimated to save approximately 25 million elements for each isolated IGE case and 32 million elements for each side-by-side IGE case. For side-by-side rotor cases, a box-shaped refinement region is prescribed between the rotors with elements 25% blade chord in size. The box extends 0.75R in both directions hub-to-hub, 2R in both directions normal to hub-to-hub and 2R in both directions vertically from the center point between both rotor hubs. Based on the results in the appendix, this degree

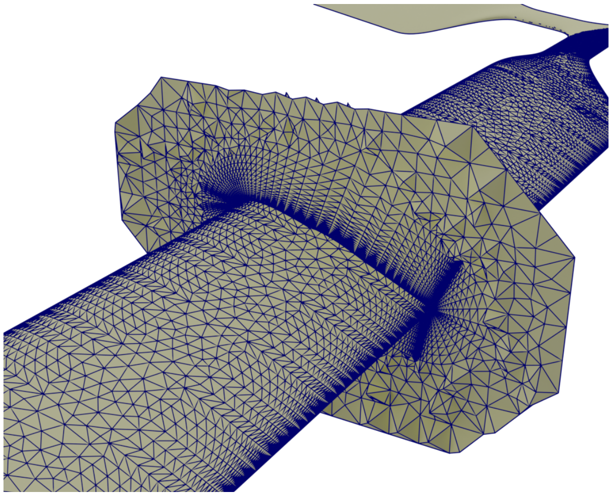

Figure 4: Blade surface mesh viewed near mid span, and a chordwise slice showing the boundary layer mesh in the wall-normal direction

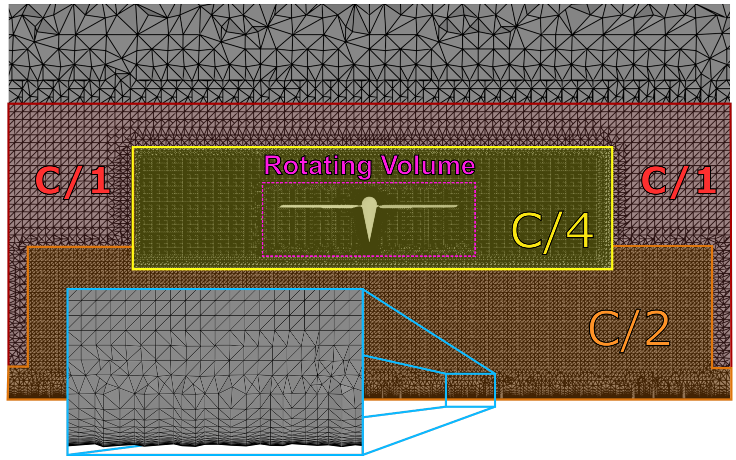

Figure 5: Cross-section of wake mesh refinement

of inter-rotor refinement is deemed to be sufficient, with integrated thrust and torque changing by less than 1.0% compared to a mesh with 12.5% blade chord sized elements in this region. The entire computational domain is comprised of approximately 170 million elements for side-by-side cases, with 50 million in each rotating volume, and 70 million in the surrounding non-rotating volume. These rotor mesh parameters have been used in previously published AcuSolve® rotorcraft simulations, and have been found to provide spatial convergence to within 1.2% integrated thrust and 1.6% integrated torque (Refs. 3, 4).

A delayed detached eddy simulation (DDES) is used with the Spalart-Allmarus (SA) turbulence model on-body for all simulations. Each case is initially run using time steps corresponding to 10° of rotation for at least 40 revolutions in order to reduce the computational cost of rotor wake development. These initial 10° time steps are possible without numerical divergence due to the stability afforded by the Streamline Upwind Petrov-Galerkin (SUPG) stabilized finite element method and generalized α implicit time integration method. The latter method was designed to suppress high frequency distrubances and allow solution stability with Courant-Friedrichs-Lewy (CFL) number greater than 1 (Refs. 62, 63). Following the revolutions simulated with 10° time steps, an additional 5 revolutions (at minimum) are performed with time steps corresponding to 1° with sufficient subiterations to reduced residuals by two orders of magnitude. Based on results presented in the appendix, timesteps corresponding to 1° of rotor rotation are deemed sufficient, with integrated thrust and torque differing by less than 1% to a solution computed with 0.5° timesteps. When extracting steady integrated loads, the average rotor forces and moments over the final three revolutions are considered. However, for some cases, additional revolutions must be simulated in order to more fully observe low-frequency load fluctuations. If the single revolution running averaged thrust for either rotor is found to change by more than 1% over three revolutions, additional revolutions are simulated. All runs are performed on 8 24-core AMD Epyc 7451 processors, part of the Center for Computational Innovations (CCI) at Rensselaer Polytechnic Institute.

RESULTS

Isolated Rotors in Ground Effect

As a point of reference for side-by-side rotor performance IGE, a single hovering rotor IGE at z/R = 1.0 is first simulated and its performance is compared to a rotor hovering OGE. Fig. 6 shows the difference in sectional thrust coefficient between the two cases (IGE minus OGE). Here, red represents an increase in thrust compared to OGE, and blue represents a thrust deficit compared to OGE. Thrust increment is observed on the interior of the disk (from the root to 0.85R), whereas thrust deficit is observed near the tips. Overall, integrated rotor thrust IGE at z/R = 1.0 is 6.4% greater than OGE (684.3 N IGE vs. 643.4 N OGE), making the IGE/OGE thrust ratio T_{IGE}/T_{OGE}=1.064. This ratio is similar to that predicted by Cheeseman and Bennett (T_{IGE}/T_{OGE}=1.067) (Ref. 64). The integrated rotor torque produced IGE at z/R = 1.0 is found to be within 1.2% of that produced OGE (61.3 Nm IGE vs. 60.6 Nm OGE).

The presence of a ground plane influences rotor performance by changing the wake aerodynamics. Fig. 7 shows a slice through the hub colored by vertical velocity for OGE and IGE cases with velocity direction vectors. For the OGE case, the dark blue wake freely convects downwards. When the ground plane is introduced however, the wake impinges on the ground plane. The wake's tip vortices impact the ground and spread outward radially. Inside the wake, flow is constrained by both the ground plane and the outboard wake. With nowhere to go, the inboard section of the flow fountains upwards around the hub region. Fountaining around the hub

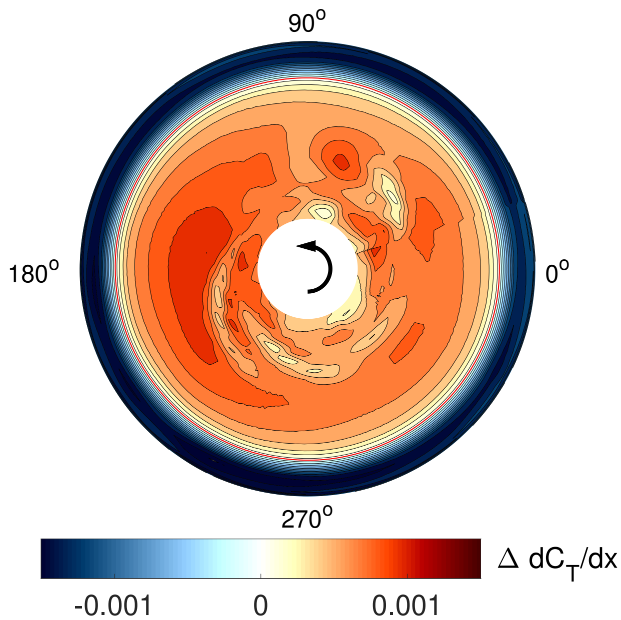

Figure 6: Sectional thrust coefficient difference between a single IGE rotor at z/R = 1.0, and an OGE rotor (IGE minus OGE)

region and through the central portion of the rotor disk has been reported on other rotors IGE and is attributed to root vortices converging to the center of rotation and traveling vertically upwards (Refs. 13, 29). Within the fountaining region, strong turbulence is observed with many vortical structures mixing and interacting.

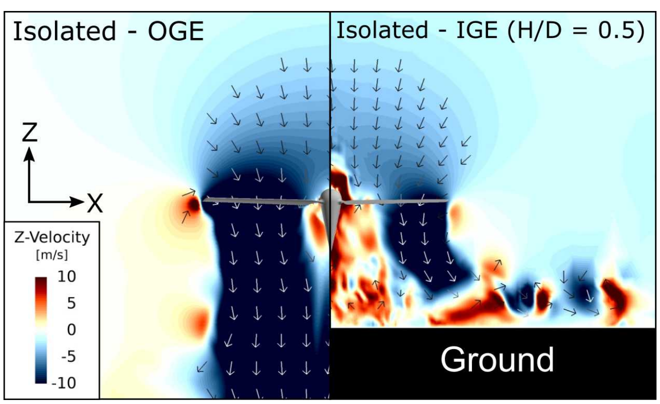

Figure 7: Slice colored by vertical velocity for OGE and IGE (z/R = 1.0) rotors

The relationship between wake structure and thrust production can be seen by looking at vertical velocity over the rotor disk. Fig. 8 shows vertical velocity at the rotor plane for OGE and IGE rotors. The vertical velocity difference between the cases (IGE minus OGE) is also shown. On the inboard sections of the blade, a positive difference in velocity is observed (orange portion of rightmost slice in Fig. 8). With the two left vertical velocity plots showing downward velocity (blue) in this region, this indicates a reduction in downwash induced by the IGE rotor (compared to the OGE rotor). Fountaining on the inboard regions of the rotor induces relative upwash on the inboard blade sections. Upwash on inboard blade sections leads to increase in angle of attack and the relative increase in thrust observed in Fig. 6. The IGE rotor shows a thrust deficit over the tip region (see dark blue peripheral ring at radial stations outboard of 85% in Fig. 6). This is a result of higher downwash at the blade tips (see dark purple region on the right slice of Fig. 8 and can be attributed to the recirculating flow IGE.

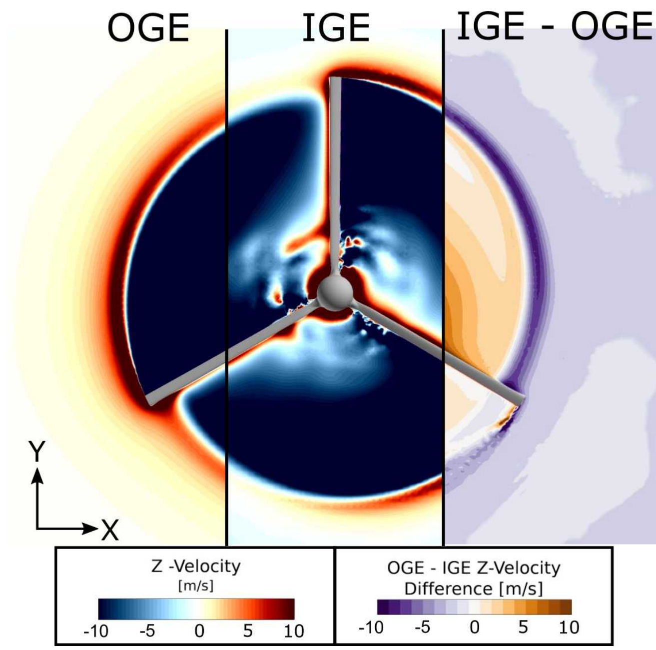

Figure 8: Vertical velocity through OGE and IGE (z/R = 1.0) rotor disks, as well as vertical velocity difference (IGE minus OGE) at the rotor plane

A canted isolated rotor is also simulated IGE with the hub positioned at z/R = 1.0. The rotor is canted 10° such that the part of the disk at $\psi = 0°$ is oriented down and the part at $\psi = 180°$ is oriented up. The sectional thrust coefficient difference between this rotor and one operating OGE is presented in Fig. 9. Like the uncanted rotor at z/R = 1.0 (Fig. 6), thrust increment is observed inboard and thrust deficit is observed near the tips. However, when the rotor is canted in Fig. 9, less thrust increment is seen on the interior part of the disk (r/R = 0% – 80%) over a majority of the azimuths. On the lower side of the disk ($\psi = 0°$), some local regions of increased thrust are observed, indicating that fountained flow passes through this part of the disk. Overall, the local thrust increment near $\psi = 0°$ does not compensate for the relatively modest thrust increment at other azimuths. Integrated over the whole disk, the canted IGE rotor only generates 3.4% more thrust than an isolated OGE rotor (665.1 N IGE versus 643.4 N OGE) which is 2.8% less thrust than an uncanted IGE rotor at the same height (665.1 N canted versus 684.3 N uncanted).

The net thrust deficit compared to an uncanted IGE rotor is explained by examining the wake profile of the canted IGE rotor. Fig. 10 plots a slice cutting through the canted IGE rotor hub colored by vertical velocity. Velocity direction vectors are also shown. With the rotor canted, the wake convects towards

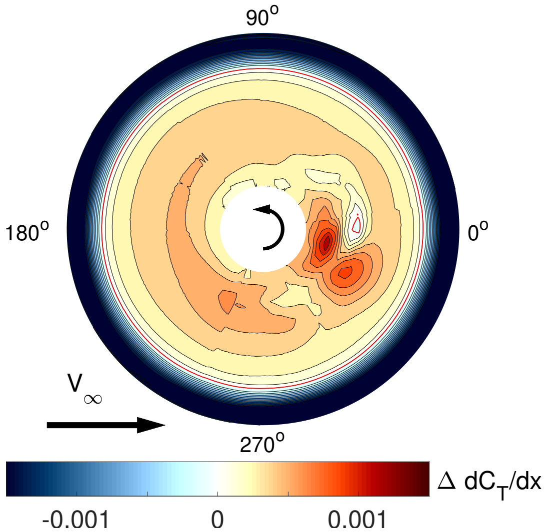

Figure 9: Sectional thrust coefficient difference between a single canted IGE rotor at z/R = 1.0, and an OGE rotor (IGE minus OGE).

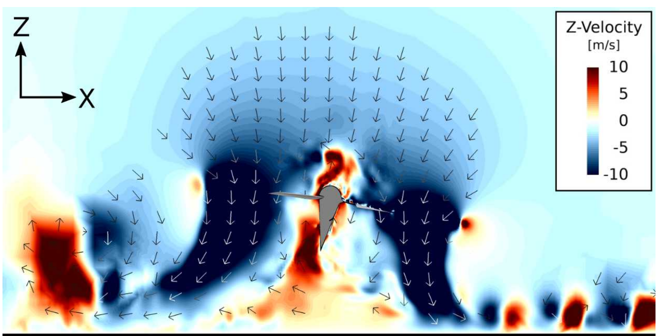

Figure 10: Slice colored by vertical velocity for a canted IGE rotor.

the ground at an angle. This allows for more wake flow to escape particularly on the left side. As a result, less upwards fountaining velocity is observed on the inboard portions of the canted rotor wake (Fig. 10) than was observed for the uncanted rotor wake (Fig. 7). This reduced amount of fountaining is responsible for the degraded thrust production in Fig. 9 as less upwash is present to increase the angle of attack on inboard blade sections. Similar findings have been reported by Tritschler, Milluzzo and Holder who show wake asymmetries for canted rotor IGE that result in increased power requirements (which is analogous to lower thrust at constant RPM) (Ref. 50).

Uncanted Side-by-side Rotors IGE

Uncanted side-by-side rotors are presented next as a point of comparison for canted side-by-side rotors IGE. Fig. 11 shows a direct volume rendering of vorticity magnitude for the uncanted side-by-side rotors. Portions of the flow-field with greater vorticity magnitude are rendered with more opacity. Tip paths for each rotor are annotated as magenta rings. A magenta grid is also plotted parallel to the $\psi = 90^\circ - 270^\circ$ line between the rotors. From $\psi = 270^\circ$ to 90° (through 0° in the direction of rotation), the right rotor wake has a similar structure to that of a single rotor. Tip vortices convect down and impact the ground, then move radially away from the rotor. On the side of the disk facing the other rotor however, the flow from the two rotors collide and the flow is constrained from moving radially. Where the wakes collide, mixing produces a wall of strong turbulence between the rotors, in the inter-rotor region. This wall extends upwards and outwards (laterally) and intersects the tip-path-plane of the rotors (covering both the magenta tip path plane rings and the middle magenta grid). Flow in this region fountains upwards and also exits outwards laterally in the direction normal to a line connecting both rotor hubs. Similar effects have been observed on tiltrotors in hover, where spanwise flow over the wing has been shown to fountain over the centerline of the vehicle and fluctuate left and right over many revolutions. Reingestion of the fountained flow has been reported to reduce rotor performance near the tips and induce impulsive loading (Refs. 34–37). In this case, however, the extents of the ground plane are not limited to the chordwise extents of a wing, and so the region of fountaining flow extents farther outward laterally than that observed on tiltrotor wings.

Fig. 12 shows the difference in sectional thrust coefficient between the two IGE rotors and an OGE single rotor (IGE minus OGE), phase averaged over three revolutions. Thrust increment inboard, and thrust deficit outboard are observed like with the single uncanted rotor IGE case. However, with the presence of two rotors, larger thrust losses are observed at the tips when the blades pass between the rotors (compare the region around ψ=180° on the right rotor in Fig. 12 to the region around ψ=0°). On the right rotor at ψ=180°, dC_T/dx is 0.0038 less than an isolated OGE rotor, whereas at ψ=0°, dC_T/dx is only 0.0014 less. Similar inter-rotor thrust deficits have been reported for close proximity rotors OGE, but these effects have been shown to be small, reducing integrated thrust by less than 2% (Refs. 9, 65). Inter-rotor thrust losses are greater IGE, with dC_T/dx between the rotors reducing by up to 39.9% (compared to if the rotor was operating in isolation). The losses are also dissimilar in distribution between the rotors, and change from revolution to revolution due to the highly chaotic vortical flow in the inter-rotor region.

The unsteady thrust produced by side-by-side rotors IGE suggests interactional aerodynamics between the rotors. Fig. 13 shows a slice cutting through both rotor hubs colored by vorticity in the +Y direction (into the page). Velocity direction vectors are also shown. On the outsides of the system, tip vortices are observed to move downwards, then outward radially upon impacting the ground (similar to a single rotor IGE). Between the rotors however, substantial wake mixing is observed. The wakes of each rotor collide in the middle to produce a highly turbulent vortical flow with substantial mixing. As each blade passes through the inter-rotor region, it intersects with the vortical flow between the rotors. Tip vortices generated between the rotors are pulled into the mixing region, adding vorticity to the flow and perpetuating the turbulent nature of the region. Turbulent mixing flow fountains above the rotors and intersects with the disk planes. As the

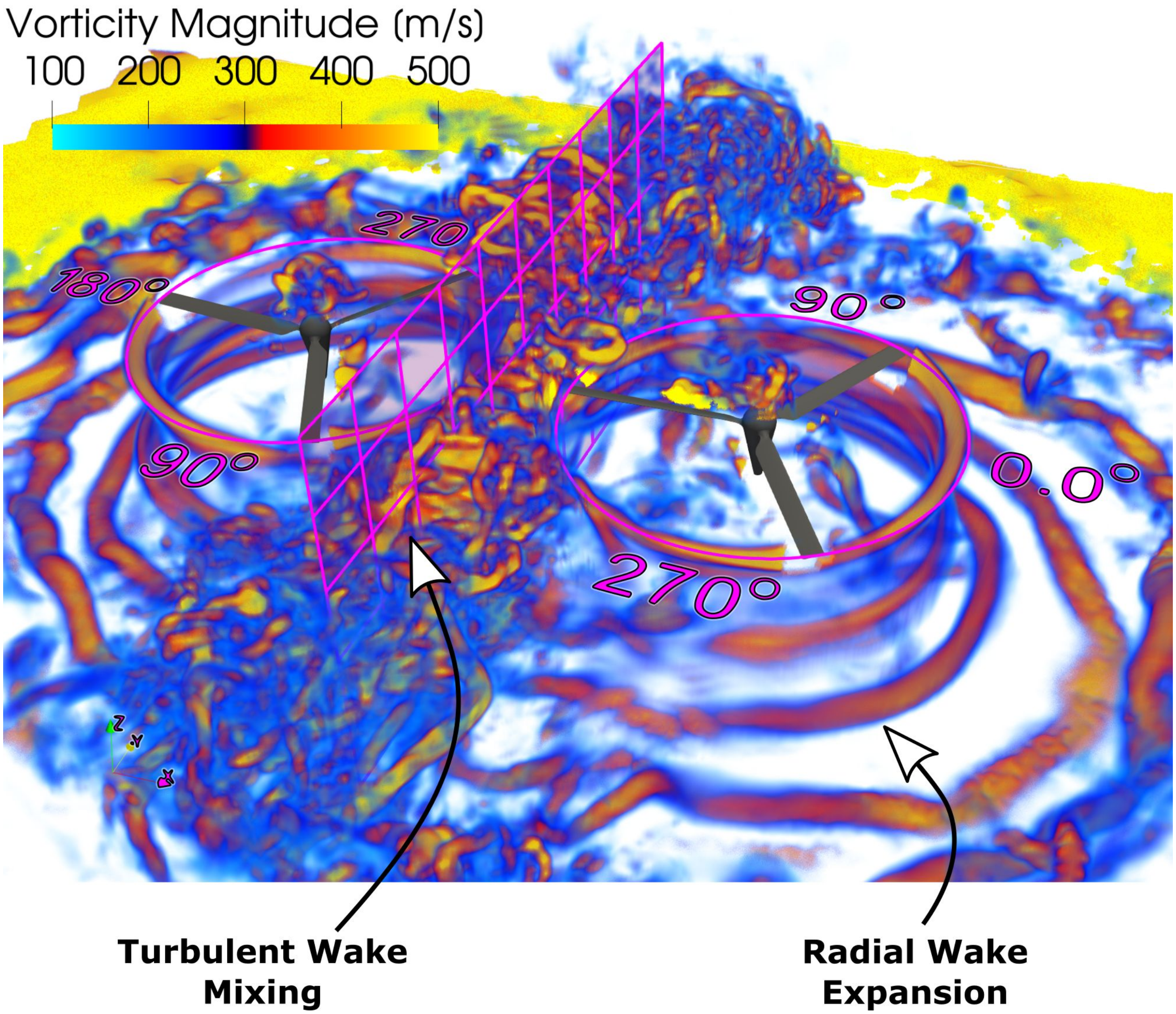

Figure 11: Direct volume rendering of uncanted side-by-side rotors with opacity and color dictated by vorticity magnitude

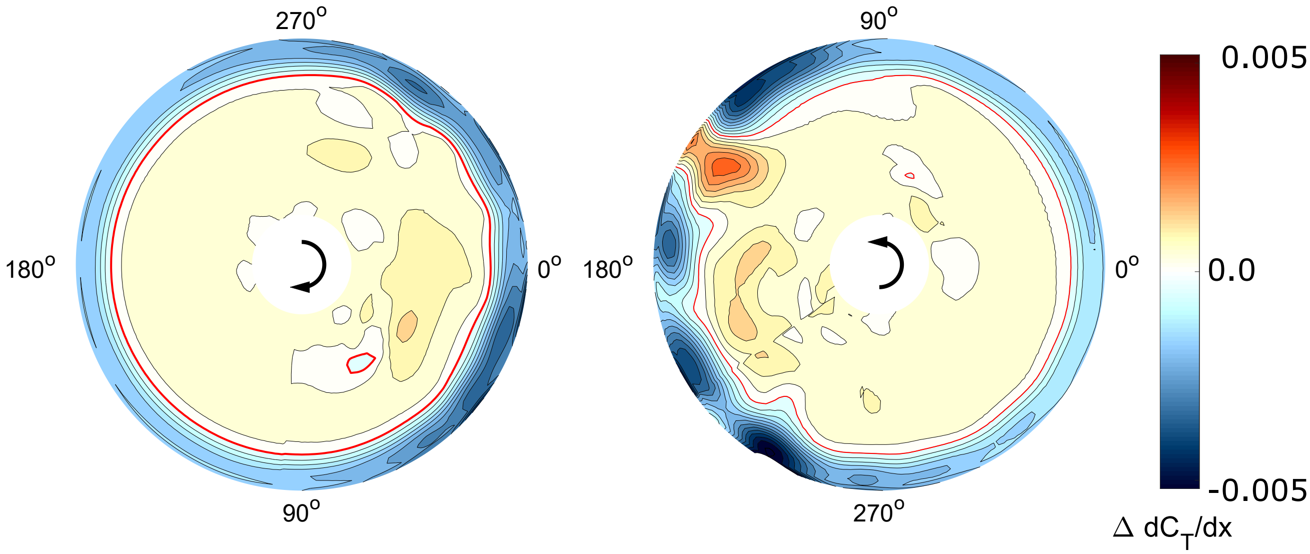

Figure 12: Three revolution average sectional thrust coefficient difference between uncanted side-by-side rotors IGE and a single OGE rotor

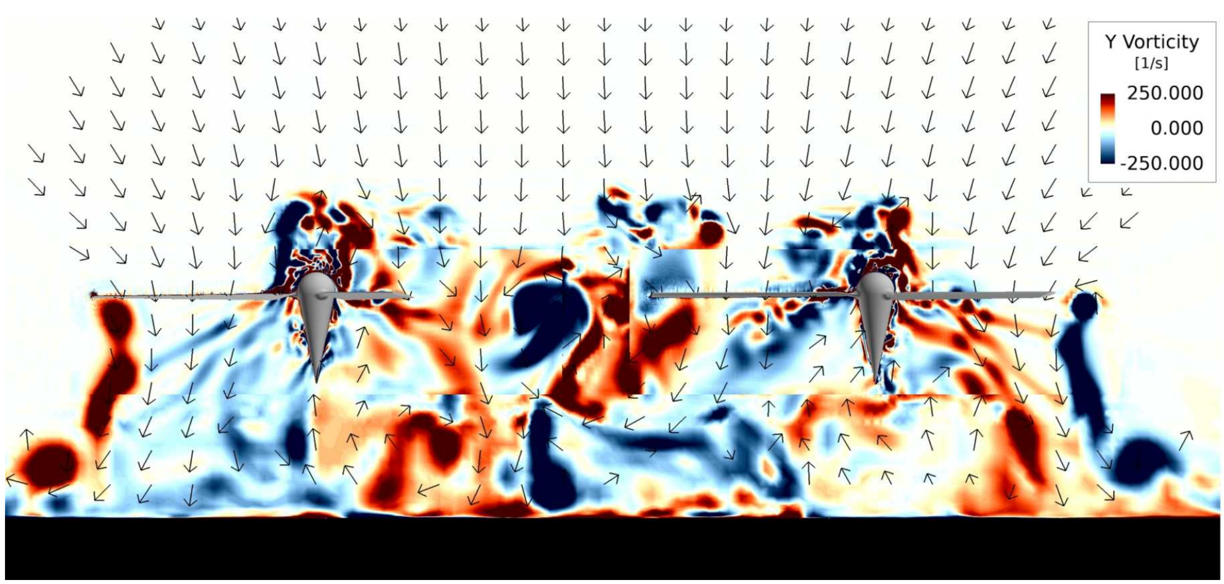

Figure 13: Slice cutting through uncanted side-by-side IGE rotor hubs colored by Y-vorticity (into the page)

blades pass through the turbulent mixing, impulsive loading is induced.

Fig. 14 shows the thrust history for each uncanted side-by-side rotor normalized by isolated OGE rotor thrust. Running average thrust over one revolution is also presented for each rotor, as well as average thrust between the two rotors. Substantial vibratory loading is observed for both rotors as blades pass through the center mixing region, with peak-to-peak fluctuations in excess of 16% the steady thrust. Average thrust over one revolution is not steady, with the left rotor average thrust changing by 4.8% over the revolutions plotted (and the right rotor changing by 2%). The relative mean thrust between rotors changes as well, with the left rotor producing more thrust at certain revolutions, and the right rotor producing more at others. The relative lift share between the two rotors depends on the predominant position of the unsteady vortical flow in the inter-rotor region, with a rotor producing more thrust when the majority of turbulence drifts away from it (Ref. 43). Average thrust of both rotors is relatively stable, changing by approximately 2% over these nine revolutions. Overall, the thrust increment gained inboard is somewhat canceled by thrust deficits incurred between the rotors. Averaging over three revolutions (and averaging between both left and right rotors), the uncanted side-by-side rotors produce 4.3% more thrust than a single rotor OGE (670.8 N IGE vs. 643.4 N OGE), but 2.4% less thrust than an isolated rotor at z/R = 1.0 (670.8 N side-by-side vs. 687.5 N isolated).

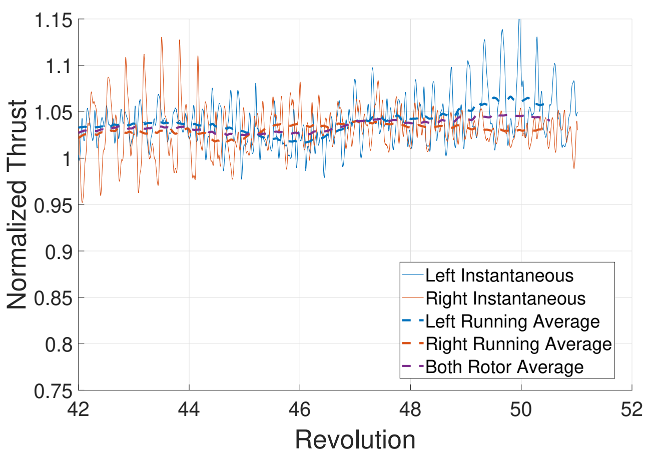

Figure 14: Thrust history of each uncanted side-by-side rotor IGE, including instantaneous, single rotor rev-averaged thrust and both rotor rev-averaged thrust normalized by isolated OGE thrust

Laterally Canted Side-by-side Rotors IGE

When the rotors are canted laterally, the wakes of each rotor are tilted in opposite directions. Fig. 15 shows a direct volume rendering of vorticity magnitude for the laterally canted rotors. Despite the wakes of each rotor being reoriented, many of the same characteristics seen in Fig. 11 are present. Parts of the wake positioned far from the other rotor ($\psi = 270°$ through $0°$ to $90°$ for the right rotor) spread radially along the ground as if in isolation. An increased number of secondary vortices are observed around each of the laterally canted tip vortices. Comparing the vorticity around $\psi = 0°$ for the right rotor in Figs. 11 and 15, the uncanted rotors show clean primary tip vortices, whereas those generated by the laterally canted rotors show additional secondary vortices wrapping around the primary tip vortices. Between the rotors, each wake still collides, forming a turbulent mixing region that extends from the ground to over the disk planes.

For the laterally canted rotors, the high vorticity flow is still observed between the rotors, though it is somewhat shifted towards parts of the disks that are oriented low to the ground (around $\psi = 240°$). This can more clearly be seen in Fig. 16 which plots an unwrapped cylinder extending from the ground plane to a height of z/R = 2.0 around an isolated rotor or the right rotor of a two rotor system. The colors indicate the instantaneous vorticity magnitude. The cylinder radius extends 1.25R and therefore reaches the middle (symmetry plane) of the side-by-side rotor systems at $\psi = 180°$. The cylinder (diagrammed in the bottom-left) is unwrapped to form a 2D plane. A cyan line is plotted along the projection of the tip path plane on the cylinder. For the uncanted side-by-side rotors, the high vorticity flow caused by wake mixing is centered about $\psi = 180°$. For the laterally canted rotors however, high vorticity flow is skewed towards $\psi = 240°$ where the tip path plane lies closer to the ground. Increased levels of turbulence near low-passing blade tips can be attributed to the wake flow being younger (and therefore stronger) when it interacts with the wake of the other rotor.

Fig. 17 shows the sectional thrust coefficient difference between the laterally canted side-by-side rotors IGE and isolated OGE rotors (IGE minus OGE). Like the uncanted side-by-side rotors, turbulent mixing between the rotors leads to thrust deficit near the tips at $\psi = 0°$ for the left rotor and $\psi = 180°$ for the right rotor. However, the inter-rotor thrust deficit for these laterally canted rotors is biased towards the side that is tilted down. On the left rotor, additional thrust deficit is observed near $\psi = 300°$, coinciding with where strong turbulent flow was observed in Fig. 15. Each rotor is tilted with $\psi = 270°$ down, and so additional thrust deficit is seen at $\psi = 240°$ (also where turbulent flow was seen in Fig. 15). In general, the wake from portions of the rotor disk that are on the side facing the other rotor and also tilted closer to the ground generate increased levels of turbulent mixing. The tip path planes pass through these regions of increased vortical flow, particularly because they are positioned closer to the ground where the mixing is strongest. Therefore, the tilted downwards inter-rotor disk regions show additional thrust deficit compared to parts that are lifted up, away from the ground. Furthermore, less thrust increment is observed inboard than the uncanted rotors in Fig. 12 due to the tilted orientation of the rotors (similar to the isolated canted rotor in Fig. 9).

Blades passing through flow with greater levels of turbulence also increases unsteady loading. Fig. 18 shows the thrust history for each laterally canted side-by-side rotor normalized by isolated OGE rotor thrust. Running average thrust over

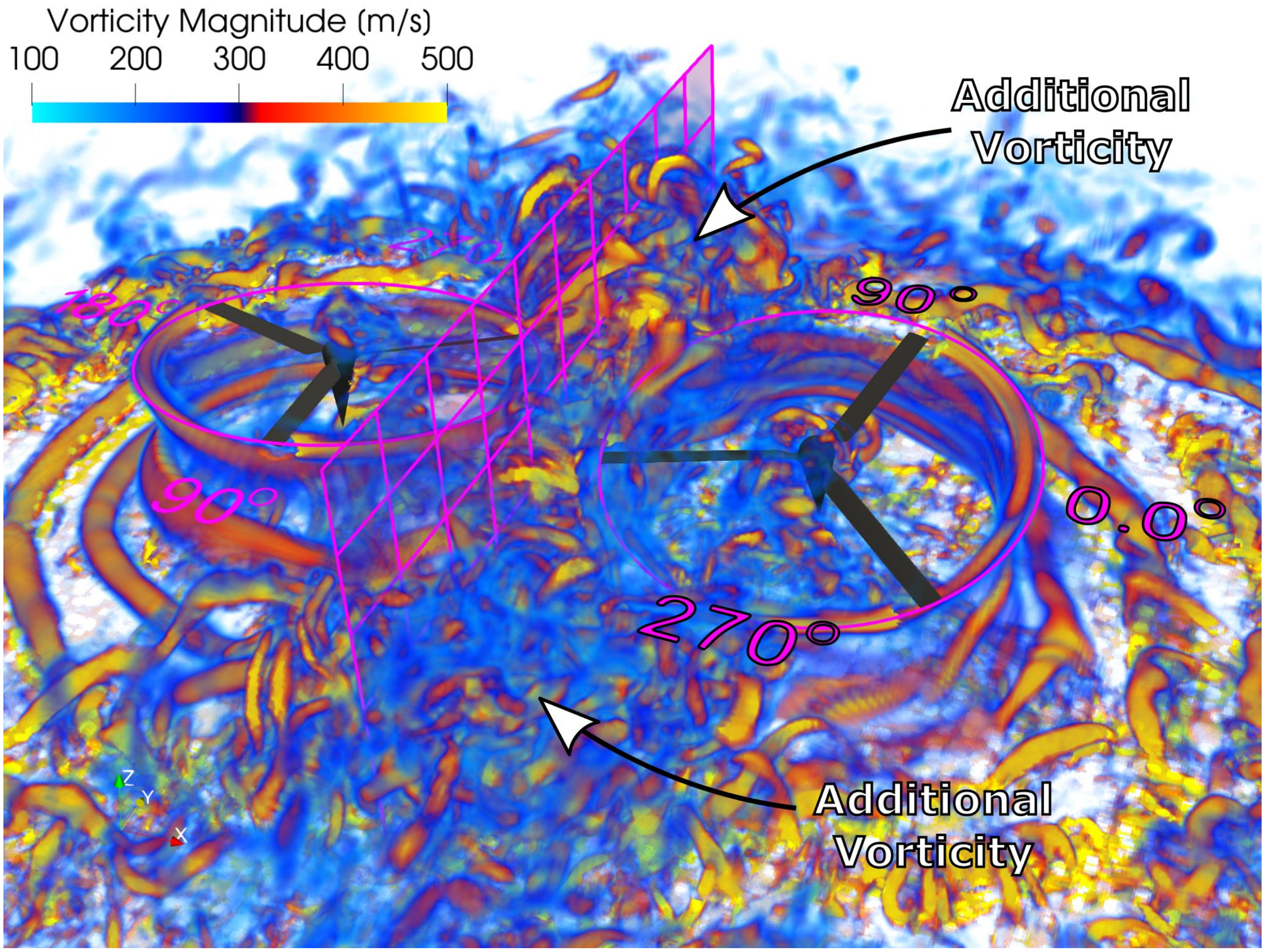

Figure 15: Direct volume rendering of laterally canted side-by-side rotors with opacity and color dictated by vorticity magnitude

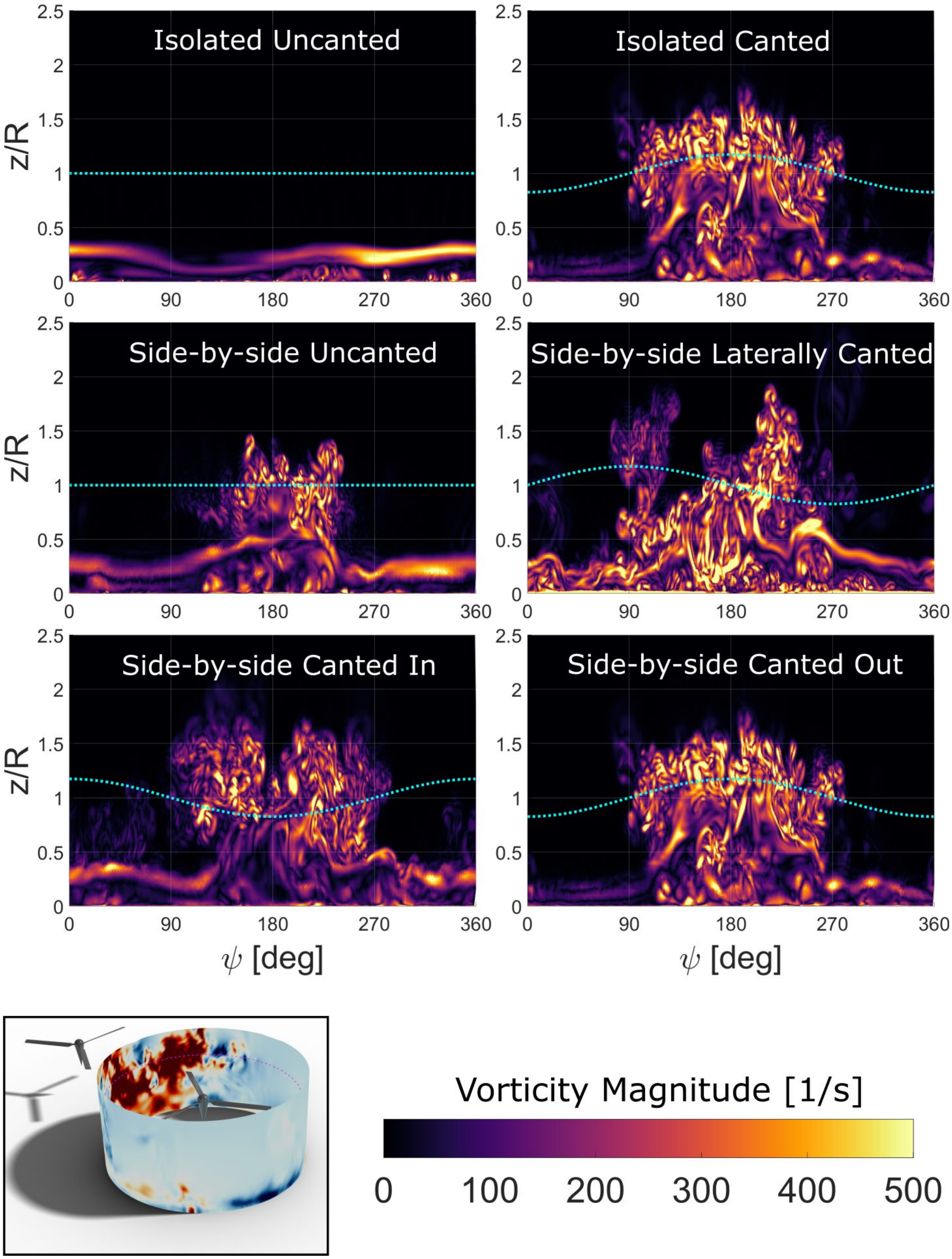

Figure 16: Unwrapped cylinders colored by vorticity magnitude for canted and uncanted isolated rotors as well as for the side-by-side rotors described in Fig. 2

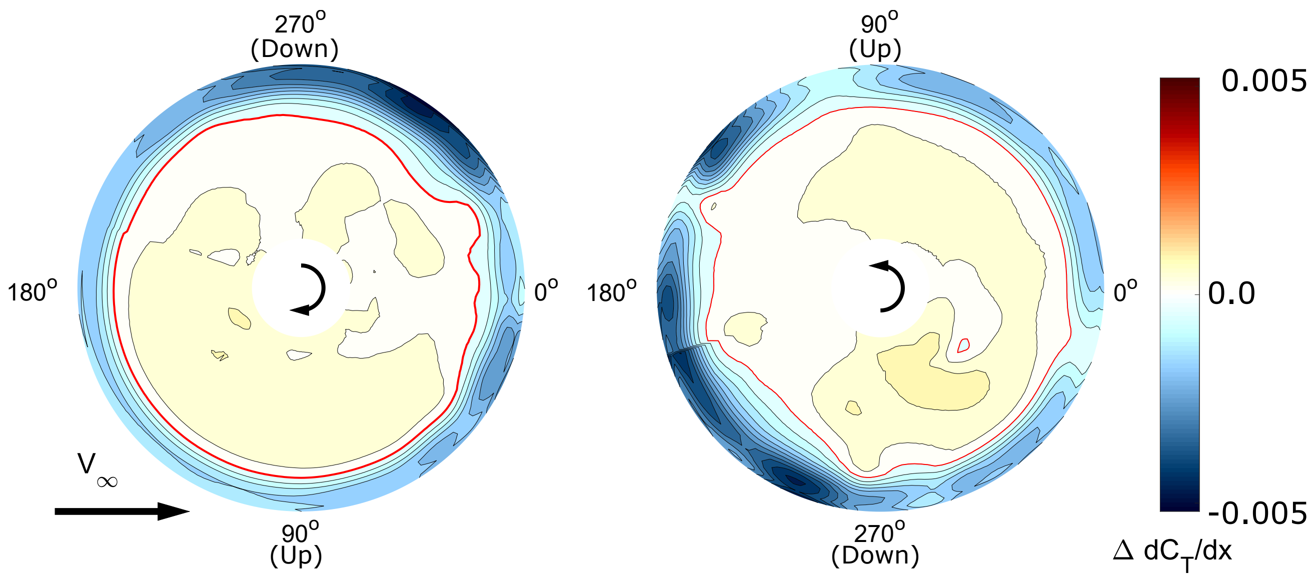

Figure 17: Three revolution average sectional thrust coefficient difference between laterally canted side-by-side rotors IGE and a single OGE rotor

one revolution is also presented for each rotor, as well as average thrust between the two rotors. Unsteady loading for the laterally canted rotors is still much greater than for an isolated rotor operating IGE, with peak-peak thrust fluctuations reaching up to 12% the steady thrust value. The rev-averaged thrust is also still unsteady, though less so than the uncanted rotors. For these five revolutions, the right rotor average thrust changes by 2.6% and the left rotor changes by 1.3%. Overall, the additional thrust deficit incurred by parts of the disk sitting close to the ground (in addition to the reduced inboard thrust increment caused by the tilted rotor orientation) eliminates any nominal thrust increment IGE. The laterally canted rotors IGE only produce 0.6% more thrust than an isolated OGE rotor (647.2 N IGE versus 643.4 N OGE) and 5.6% less than an isolated rotor at z/R = 1.0 (647.2 N side-by-side versus 685.5 N isolated).

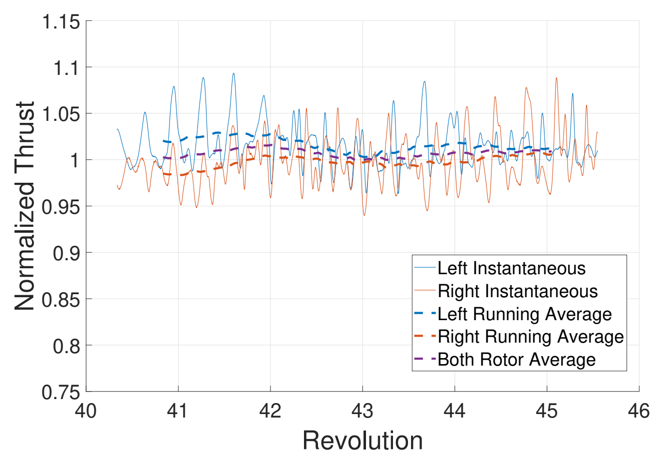

Figure 18: Thrust history of each laterally canted side-by-side rotor IGE, including instantaneous, single rotor rev-averaged thrust and both rotor rev-averaged thrust normalized by isolated OGE thrust

Canted Inwards Side-by-side Rotors IGE

Canting the rotors inwards points their wakes away from each other. However, it also brings the middle parts of the disks (ψ = 0° on the left rotor and ψ = 180° on the right rotor) closer to the ground where the wakes collide. Fig. 19 shows a direct volume rendering of vorticity magnitude for the canted inwards rotors. Again, the primary flow features are similar to those from the uncanted rotors with flow away from the other rotor spreading radially like an isolated rotor wake, and flow between the rotors forming a turbulent mixing region. In this case, the canted inwards rotors produce an inter-rotor turbulent mixing region that extends farther than that for the uncanted rotors. In Fig. 16, the high vorticity flow for canted inwards rotors extends higher and over a wider range of azimuths than it does with the uncanted rotors. Furthermore, the blades pass lower through the turbulent mixing region, exposing them to more of the unsteady flow. With the rotors exposed to a greater degree of turbulence, the interactional aerodynamic effects are strengthened.

Fig. 20 presents the sectional thrust coefficient difference between the canted inwards side-by-side rotors IGE and an isolated OGE rotor (IGE minus OGE). Outboard thrust deficit is observed across both rotor disks with bias towards the middle of the two rotors. With the rotors passing lower and closer to the strong inter-rotor vortical flow, more outboard thrust deficit is observed than was seen on the uncanted rotors in Fig. 12. Looking at inboard blade sections, uncanted rotors saw lift increment due to upwash around the hub region. For the inward canted rotors however, this inboard upwash and lift enhancement is tremendously weakened. This is potentially due to the wakes of each rotor pointing away from each other, giving a path for wake flow to escape and not fountain

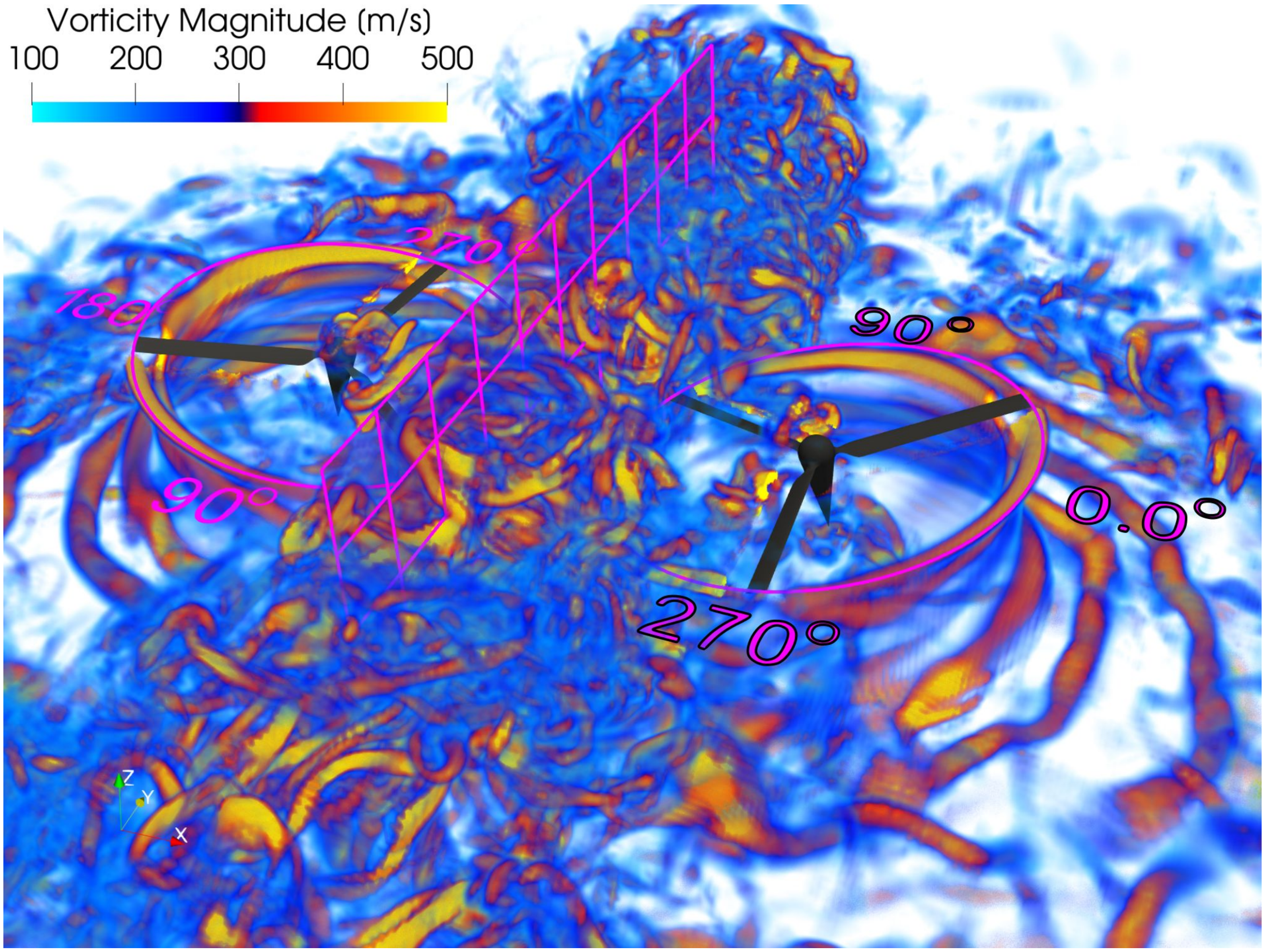

Figure 19: Direct volume rendering of canted inwards side-by-side rotors with opacity and color dictated by vorticity magnitude

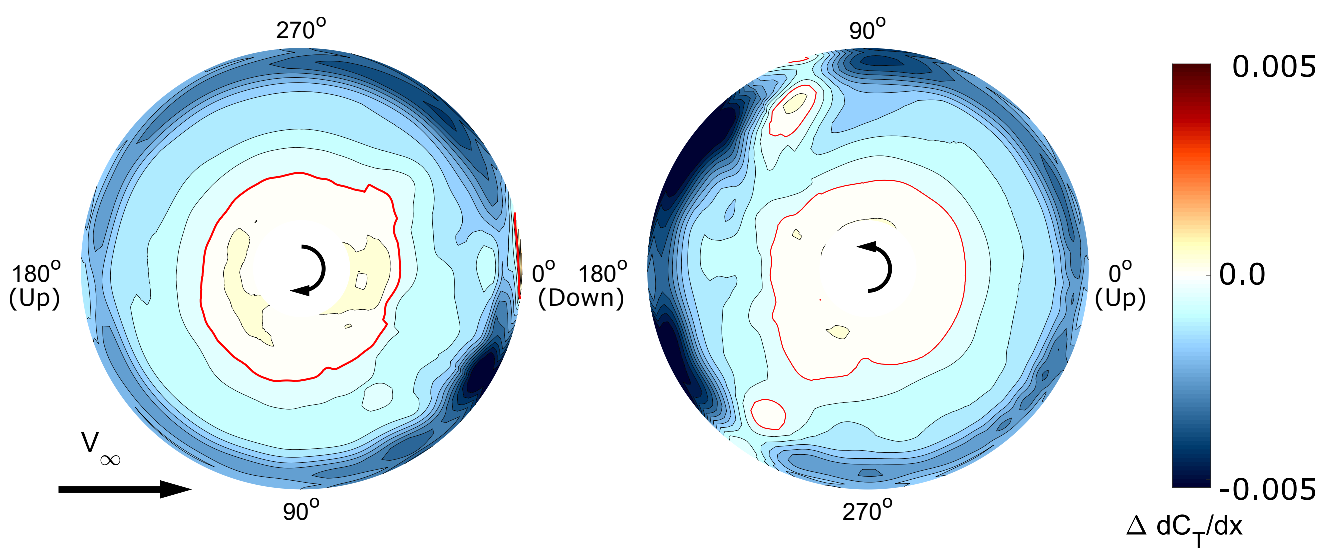

Figure 20: Three revolution average sectional thrust coefficient difference between canted inwards side-by-side rotors IGE and a single OGE rotor

up through the disk plane. Overall, each of these rotors produce 15.2% less thrust than an isolated OGE rotor (545.6 N IGE vs. 643.4 N OGE) and 20.3% less than an isolated IGE rotor at z/R = 1.0 (545.6 N side-by-side vs. 685.5 N isolated). This makes the canted inwards rotors the worst performing out of all configurations considered.

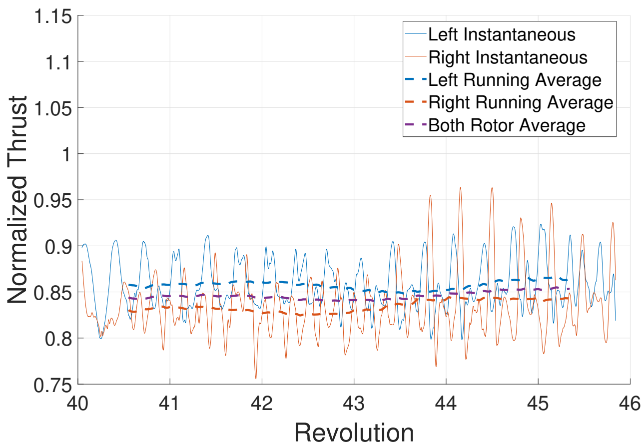

Figure 21: Thrust history of each canted inward side-by-side rotor IGE, including instantaneous, single rotor rev-averaged thrust and both rotor rev-averaged thrust normalized by isolated OGE thrust

Unsteady loading on the canted inwards rotors can be seen in Fig. 21 which shows the thrust history for each canted inward side-by-side rotor normalized by isolated OGE rotor thrust. Here, the thrust impulses are the strongest out of all cases considered, with peak-peak thrust fluctuations reaching 22% (compared to 16% for the uncanted side-by-side rotors). However, low-frequency oscillations are less pronounced with the left rotor rev-average thrust changing by less than 1.5% for these six revolutions (and the right rotor by 2.2%). Overall, with their low thrust production and strong unsteady loading, the canted inwards rotors IGE are the least favorable of those considered in Fig. 2.

Outward Canted Side-by-side Rotors IGE

Whereas the canted inward rotors places the tip paths close to the ground in the middle, canted outwards rotors lift the tip paths away from the ground there. The wake trajectory is also changed, with each rotor wake pushed towards the center of the system. Fig. 22 shows a direct volume rendering of vorticity magnitude for the canted outward rotor system. Despite the rotor wakes being pointed toward the center, portions pointing away from the other rotor still hit the ground and spread radially. Between the rotors, the colliding wakes do still generate a turbulent mixing region which in this case extends higher than with the uncanted side-by-side rotors and as high as with the canted inwards rotors. While the parts of the disks in the inter-rotor region are orient upwards, the the rotor wakes are oriented towards each other resulting in a relatively large mixing region. Despite a higher blade position in the inter-rotor mixing region, the tip path plane in Fig. 16 still passes through high-vorticity flow subjecting them to the associated interactional aerodynamic effects.

Fig. 23 shows the sectional thrust coefficient difference between canted outward side-by-side rotors IGE and an isolated OGE rotor (IGE minus OGE). The thrust change characteristics remain similar to those in Fig. 12, with some small thrust increment inboard and thrust deficit near the tips with bias towards the middle of the two rotors. Thrust increment inboard is greater than seen on laterally canted or inward canted rotors, potentially due to the inward orientation of the wakes forcing more flow upwards towards the rotor disks. Outboard, the right rotor shows more thrust deficit at $\psi = 180°$ than the left rotor does at $\psi = 0°$. Based on the findings in Ref. 43, this could be because the lifted tip paths in the inter-rotor region leaves more room for pockets of high vorticity to drift left and right. Over these three revolutions, a majority of the vorticity is positioned over the right rotor and so it loses relatively more thrust at the tips. With the greatest thrust deficit occurring at the tips of the right rotor, a greater difference in integrated thrust between the rotors is observed.

This difference can be seen in Fig. 24 which plots the instantaneous and rev-averaged thrust history for each canted outward side-by-side rotor normalized by isolated OGE rotor thrust. Here, the rev-averaged thrust history indicates how over these revolutions, the left rotor produces as much as 7.2% more thrust than the right rotor. This is indicative of low-frequency thrust oscillations present on the canted outwards rotors IGE with the right rotor rev-average thrust changing by more than 6.9% over just these six revolutions. With this in mind, it is expected that if this simulation were extended for additional revolutions, eventually the inter-rotor vorticity would move towards the left rotor, leaving the right rotor to produce the majority of the system thrust. Higher frequency thrust oscillations are also observed for these rotors, with peak-peak thrust fluctuations reaching up to 10%. This is somewhat less than the unsteady loading seen on the other side-by-side rotors IGE which showed peak-peak fluctuations ranging from 12% for the laterally canted rotors to 22% for the canted inwards rotors. Therefore, low frequency thrust unsteadiness is more characteristic of the outward canted rotors than high frequency. Overall, the thrust increment inboard for these rotors is counteracted by the inter-rotor thrust deficits (Fig. 23) leading to 0.9% less thrust produced than if they were operating in isolation OGE (637.6 N IGE versus 643.4 N OGE). Compared to an isolated IGE rotor at z/R = 1.0, the canted outwards side-by-side rotors IGE produce 7.0% less thrust (637.6 N side-by-side versus 685.5 N isolated).

INTEGRATED THRUST COMPARISON

Rotor cant and the associated interactional aerodynamics has been seen to influence the thrust production of side-by-side rotors IGE. Table 2 compares time averaged integrated thrust for all six IGE cases discussed. Thrust values are presented relative to the thrust generated by an isolated OGE rotor and are resolved in the direction of the rotor rotation vector. This

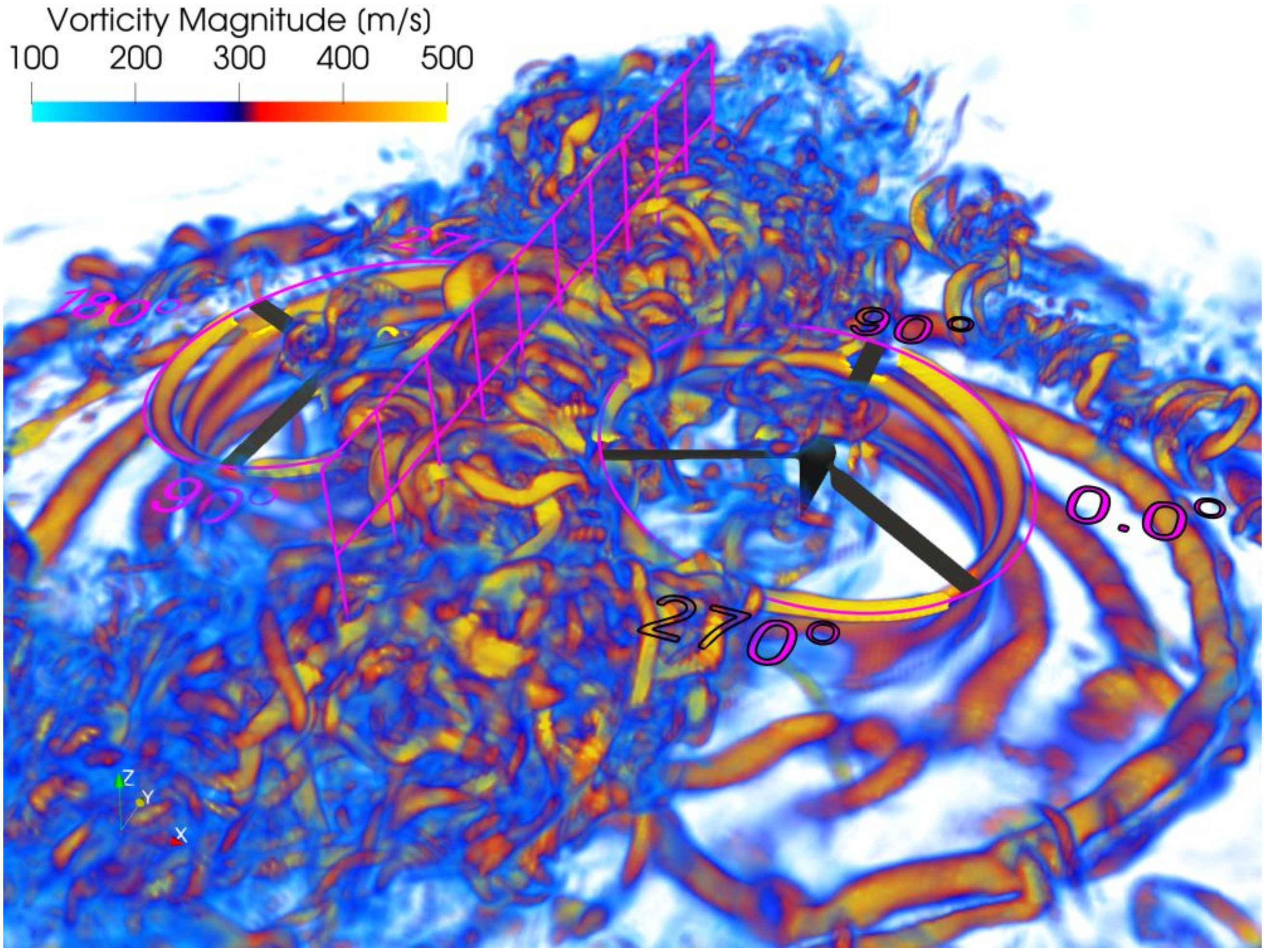

Figure 22: Direct volume rendering of canted outwards side-by-side rotors with opacity and color dictated by vorticity magnitude

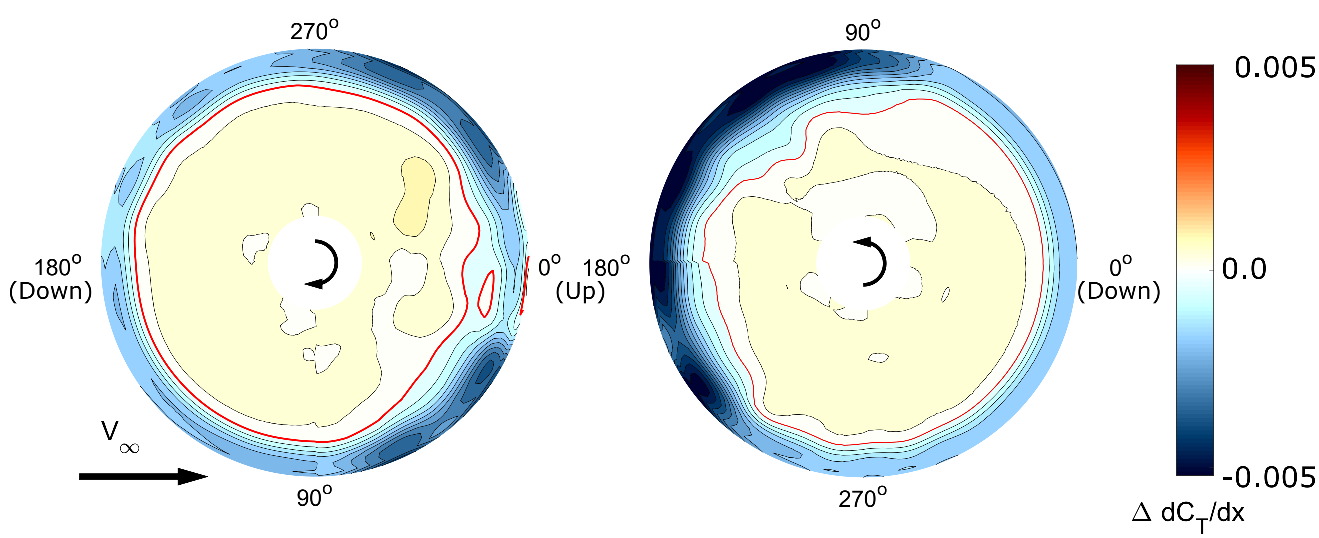

Figure 23: Three revolution average sectional thrust coefficient difference between canted outward side-by-side rotors IGE and a single OGE rotor

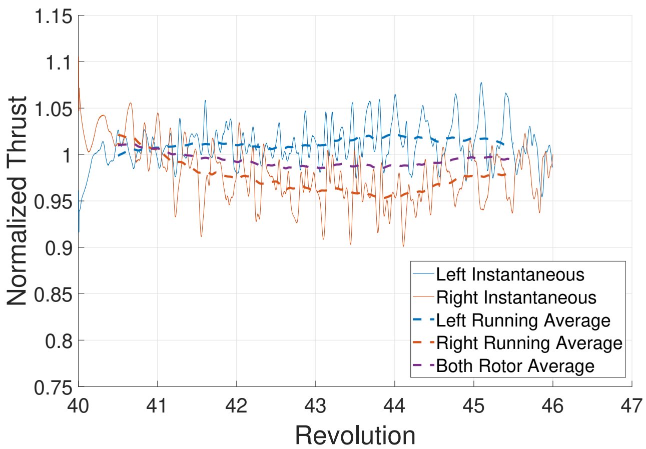

Figure 24: Thrust history of each canted outward side-by-side rotor IGE, including instantaneous, single rotor rev-averaged thrust and both rotor rev-averaged thrust normalized by isolated OGE thrust

means that the reduced vertical force from a tilted thrust vector is omitted and only interactional aerodynamic effects are responsible for the reported thrust changes.

An isolated rotor at z/R = 1.0 provides the greatest thrust increase, producing 6.4% more thrust than if OGE. Uncanted side-by-side rotors at the same z/R = 1.0 produce slightly less thrust (4.3% more than OGE) due to larger thrust deficits incurred by outboard blade sections passing through the middle turbulent mixing region. Even resolving thrust in-line with the rotation axis, the uncanted rotors produce more thrust than any of the canted rotor configurations. When an isolated rotor is canted IGE, there is less upwash around the hub region and so the thrust increment is reduced (3.4% more than OGE compared to 6.4% if uncanted). Out of the three cant directions, laterally canted side-by-side rotors generate the most thrust, though only 0.6% more than isolated rotors OGE. Canted inwards side-by-side rotors generate the least thrust (15.2% less than isolated OGE rotors) as there is no thrust increment inboard as well as large thrust deficits outboard between the rotors. Canted outwards rotors fair somewhat better, only generating 0.9% less thrust than if isolated OGE. While thrust deficits are still observed outboard on the disks, there is inboard thrust increment comparable to the isolated canted rotor. Overall, canted rotors in any direction leads to less thrust generation than if the rotors are uncanted, but if rotor cant is required for improved control authority, laterally canted rotors generate the most thrust.

Table 2: Relative thrust difference between six IGE rotor cases and isolated rotors OGE (IGE minus OGE)

Isolated Uncanted	6.4%
Isolated Canted	3.4%
Uncanted Side-by-side	4.3%
Laterally Canted Side-by-side	0.6%
Canted Inwards Side-by-side	-15.2%
Canted Outwards Side-by-side	-0.9%

Side-by-side rotor operation IGE is also associated with notable unsteady loading. The degree of unsteady loading is compared between the cases considered in Fig. 25 which plots a frequency domain decomposition of integrated rotor thrust for each case. Here, the isolated rotors both IGE and OGE produce relatively little unsteady loading across the frequency spectrum. Once two rotors are positioned in close proximity, unsteady loading is observed primarily at the 3/rev and 6/rev frequencies. The Uncanted side-by-side rotors produce 3/rev loading with an amplitude 1.25% the mean thrust. This is caused by each of the three blades passing through the inter-rotor region and incurring a single impulsive load. A similar magnitude 3/rev loading is also seen for the laterally canted and canted outward side-by-side rotors. The canted inwards rotors however produce substantially stronger unsteady loading, with the 3/rev amplitude reaching 2.8%. This is caused by the blades passing low to the ground through the inter-rotor mixing region where turbulence is strong. Not only does this reduce the integrated rotor thrust (Table 2) but it will also accelerate rotor fatigue. Unsteady loading for these rotors is also relatively high at the 6/rev frequency indicating that the blades also see multiple strong impulses as they pass through the turbulence. Unsteady loading at the 6/rev frequency is also relatively high for the laterally canted rotors. This is consistent with the wide range of azimuths over which the rotor disks in Fig. 15 intersected with vortical flow. With the blades encountering turbulence over a range of azimuths, there is a greater chance that multiple impulsive loads are induced on the blade. In general, side-by-side rotors IGE produce increased 3/Rev and 6/rev loading over isolated IGE rotors, with inward rotor cant exacerbating this effect.

Outwash Comparison

When the wake of an isolated rotor IGE impacts the ground, it is able to freely convect radially away from the rotor. As the wake skirts along the ground, it induces a net radial velocity. This can be seen for an uncanted isolated rotor in the top-left of Fig. 26. This figure plots an unwrapped cylinder extending from the ground plane to a height of z/R = 2.5 around an isolated rotor or the right rotor of a two rotor system. The colors indicate the magnitude of the instantaneous radial velocity (positive away from the rotor hub). The cylinder radius extends 1.25R and therefore reaches the middle (symmetry plane) of the side-by-side rotor systems at ψ = 180°. The cylinder (diagrammed in the bottom-left) is unwrapped to form a 2D plane. A magenta line is plotted along the projection of the tip path plane on the cylinder. Unwrapped cylinders are presented for all IGE cases considered in this study including: uncanted and canted isolated rotors as well as the side-by-side rotor systems described in Fig. 2. For the uncanted isolated rotor (top-left), a skirt of radial velocity exceeding 20 m/s is observed from the ground to z/R = 0.25.

When a second, nearby rotor is introduced (in the uncanted side-by-side configuration), the wakes of each rotor interfere with each other. Between the rotors (ψ = 135° - 240°), flow is somewhat constrained from moving radially outward along

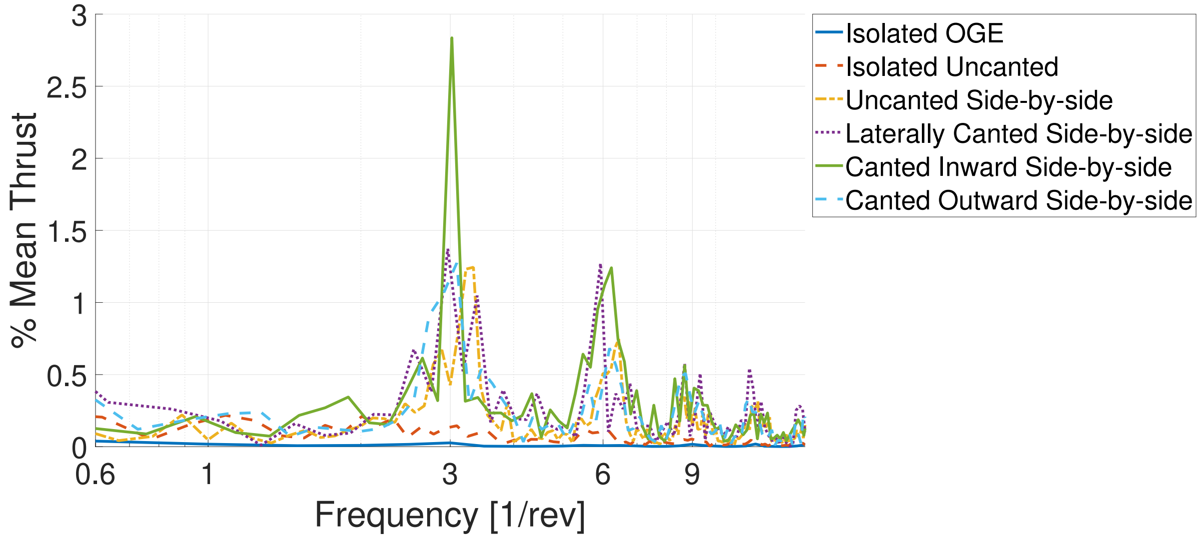

Figure 25: Frequency domain decomposition of integrated thrust for isolated rotors and side-by-side rotors considered in Fig. 2

the ground by the wake of the other rotor. Wake mixing leads to the radial velocity being bidirectional (into or out of the cylinder). Away from the other rotor, (ψ=270° - 360° and 0° - 90°), the same radial velocity is seen as with the isolated rotors. A skirt of radial velocity flows from the ground to z/R = 0.25 and is relatively uniform in height and strength.

When the rotors are laterally canted, evidence of wake mixing (flow into and out of the cylinder) is still observed between the rotors (ψ = 135° - 240°). However, mixing flow particularly around ψ = 240° extends higher than for the uncanted side-by-side rotors, extending higher than z/R = 1.75 (also seen in Fig. 16). It is this extra turbulence on the lower side of the rotor disk that is responsible for the biased thrust deficit in Fig. 17. Away from the other rotor (ψ=270° - 360° and 0° - 90°) the wake profile is similar to the uncanted rotors with a skirt of radial velocity extending from the ground to about z/R = 0.25.

For the canted inwards rotors, the radial velocity below the raised rotor sections extends somewhat higher, reaching z/R = 0.35. At ψ = 120°, near where the tip path plane is low, but outside of the mixing region, the radial wake skirt is lower, sitting below z/R = 0.25. Between the rotors, evidence of wake mixing is also observed from ψ = 120° - 270° that extends up to z/R = 1.75.

On canted outwards rotors, the sides of the disk facing away from the left rotor are positioned lower. Therefore, the radial wake skirt on this portion of the disk (ψ=270° - 360° and 0° - 90°) also sits lower, with more of the wake being directed towards the center of the system. Where the wakes collide, around ψ = 180°, evidence of turbulent mixing has similar extents to the canted inwards rotors, reaching up to z/R = 1.75. In general, inter-rotor turbulence extends higher and over a wider range of azimuths when the rotors are canted. Additionally, rotor canting directs the orientation of the wake, thereby causing the radial outwash along the ground to be biased towards the side of the disk that is oriented upward. Intuitively, ground observers will feel more rotor-induced velocity if positioned in the direction that the wake is oriented.

CONCLUSIONS

This study investigates the interactional aerodynamics of canted side-by-side rotors in ground effect. The computational fluid dynamics code AcuSolve®, with DDES, is used to simulate the aerodynamics of the system. The sliding mesh method is used to simulate blade motion by interfacing two rotating volumes (one for each rotor) within a nonrotating volume. Every simulation is performed with 5.5 ft diameter, 3 bladed rotors with uniform planform and linearly twisted blades spinning at 1600 RPM, corresponding to a 5 lb/ft^2 target disk loading OGE. In all, seven cases are simulated: isolated OGE, isolated uncanted and 10° canted IGE, and side-by-side rotors with no cant, 10° differential lateral cant, 10° cant inward and 10° cant outward. All IGE cases are performed at z/R = 1.0 and side-by-side rotors are separated by 2.5R hub-hub. The performance of isolated and side-by-side rotors IGE is compared to the performance of an isolated OGE rotor. Through these simulations, the following observations are made:

1. Between side-by-side rotors IGE (canted or uncanted), the wakes of each rotor collide, inducing turbulent mixing that can fountain up, through, and over the rotor disk plane.

2. As blades pass through the inter-rotor turbulent flow, unsteady loading is induced and a thrust deficit is incurred.

3. Canted rotors IGE (either isolated or side-by-side) generate less thrust than their uncanted counterparts due to reduced upwash around inboard blade sections.

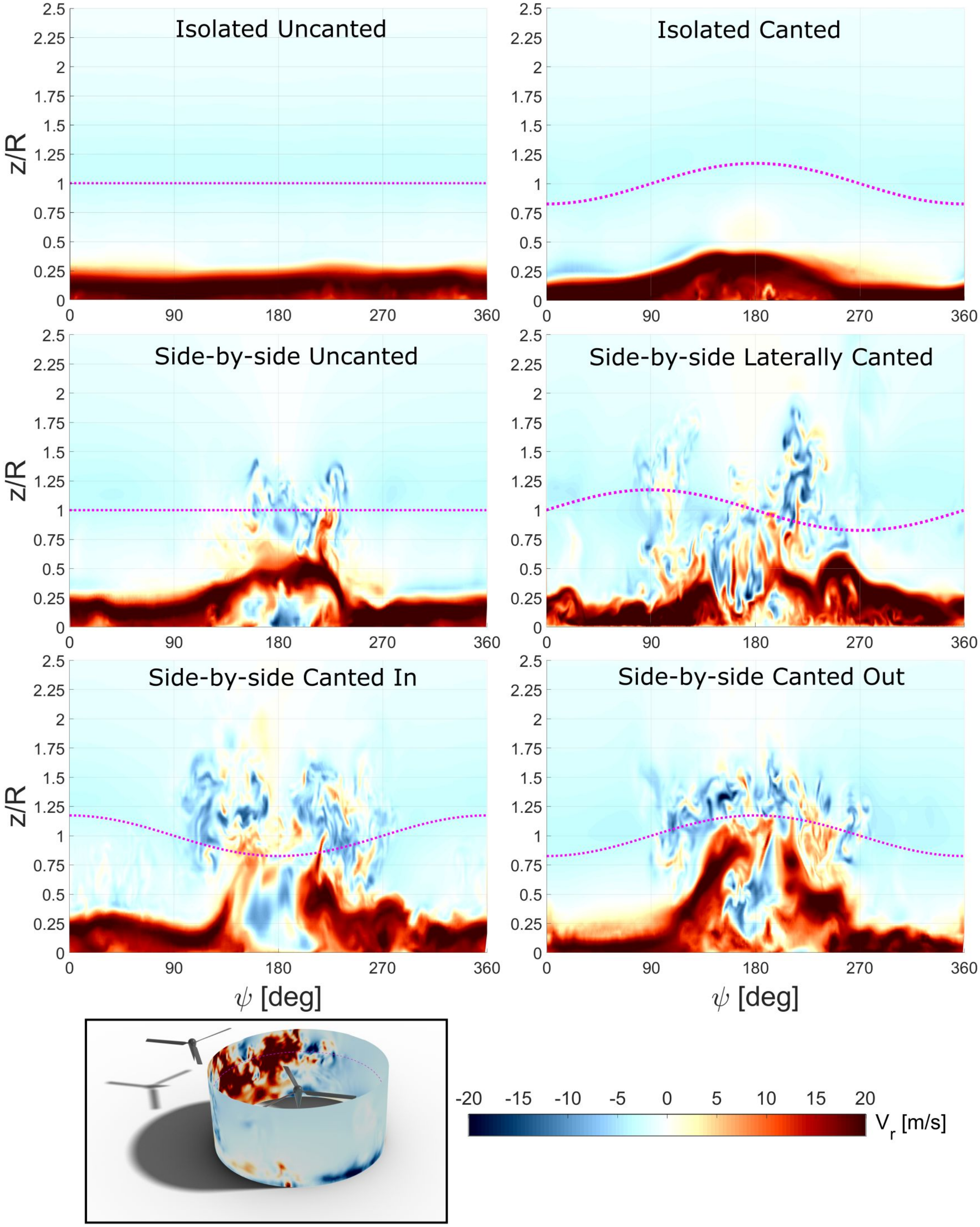

Figure 26: Unwrapped cylinders colored by radial velocity for canted and uncanted isolated rotors as well as for the side-by-side rotors described in Fig. 2

4. Laterally canted rotors IGE produce the most thrust out of each cant direction, with inter-rotor thrust deficits only shifting azimuthally towards downwards parts of the disks.

5. Canted inwards rotors generate the least thrust IGE with very little inboard thrust increment and strong inter-rotor thrust deficits. Unsteady loading is also high, reaching 22% peak-to-peak compared to 16% uncanted.

6. Canted outwards rotors produce similar thrust to isolated OGE rotors, though show more low-frequency thrust fluctuations than other cant directions.

7. The skirt of radial outwash beneath canted rotors IGE tends to extend slightly higher off the ground below raised portions of the disk.

APPENDIX

Mesh Refinement Study

For side-by-side rotors in ground effect, the region between the rotors where the wakes collide is found to contain highly turbulent flow. This turbulence is encountered by the blades as they pass through the inter-rotor region inducing impulsive loading. In order to ensure spacial convergence for this important region, a mesh refinement study was performed in which the element size in the inter-rotor region is tested at two levels: 0.25 blade chord (C/4) and 0.125 blade chord (C/8). Side-by-side rotors IGE at z/R = 1.0 with 3.0R hub-hub separation are simulated with both levels of refinement and the predicted loads are compared. A slice of each mesh is shown in Fig. 27 with the C/4 refinement mesh containing about 120 million elements and the C/8 refinement mesh containing over 195 million.

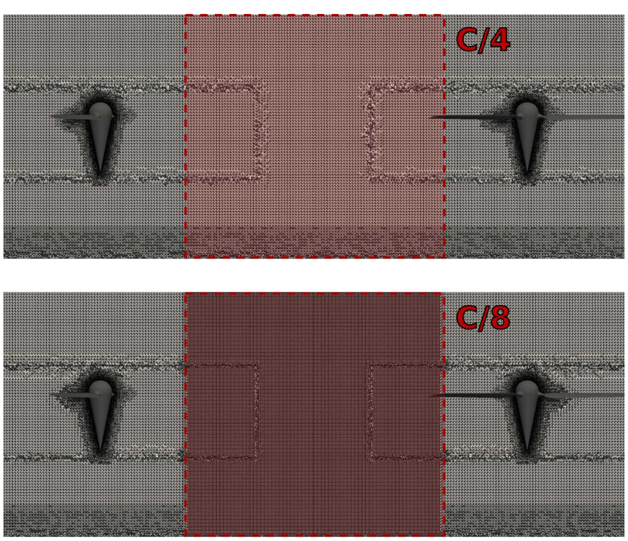

Figure 27: Crinkle-cut slice through both rotor hubs of meshes with C/4 and C/8 inter rotor mesh refinement

While the individual rotor thrust and torque are unsteady with time (as seen in Fig. 14), the both-rotor average is relatively steady and can be compared between cases. Table 3 reports the mean integrated thrust and torque of both rotors averaged over 3 revolutions. The grid with C/4 refinement shows good agreement to the grid with C/8 refinement, with thrust and torque matching to within 1%.

Table 3: C/4 and C/8 grid loads

Refinement Level	Thrust	Torque
C/4	642.9 N	60.80 N
C/8	639.1 N	60.20 N
% difference	0.6	1.0

In addition to the average loads, the unsteady loading on the blades is an important aspect to capture. Fig. 28 shows the instantaneous and rev-averaged thrust of the left rotor using C/4 and C/8 refinement. Although the stochastic nature of the turbulent mixing region leads to instantaneous thrust differences, the frequency and amplitude of the thrust time histories appear to agree well. Instantaneous thrust ranges from 601.8 N - 707.3 N over these revolutions with C/8 refinement, whereas it ranges from 589.1 N - 690.9 N with C/4 refinement (a difference of 2.3% and 3.0% between maximum and minimum values respectively). Rev-averaged loads also compare well, differing by less than 1.5% for 95% of the simulation, and showing similar low-frequency phase and amplitude.

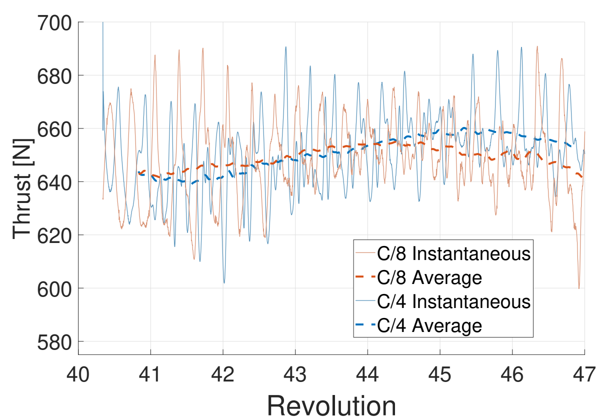

Figure 28: Left rotor instantaneous and rev-averaged thrust using C/4 and C/8 refinement

In order to better quantify the quality of unsteady loads, a fourier decomposition of the instantaneous thrust is compared between refinement levels. Fig. 29 shows this frequency decomposition of integrated rotor thrust using both refinement levels. When C/8 refinement is used, 15% stronger 3/rev and 22% stronger 6/rev content is observed than when using C/4 refinement, but both capture the peaks at 3, 6 and 9/rev. The low frequency content at 0.15/Rev also compares well between levels, with the amplitude at this frequency lying within 0.25%. Overall, the grid with C/4 refinement captures the harmonic trends of the integrated thrust signal well, and the specific n/rev amplitudes adequately, compared to using a finer grid. Considering the additional computational cost associated with a finer inter-rotor grid, C/4 is chosen as an acceptable level for identifying the general flow physics and average rotor performance for side-by-side rotors IGE.

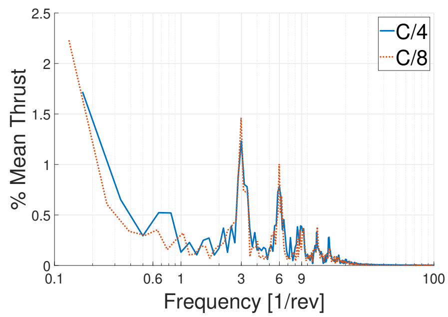

Figure 29: Frequency decomposition of integrated rotor thrust using C/4 and C/8 refinement

Temporal Refinement Study

While timesteps corresponding to 1° of rotor rotation per step has been shown to provide good predictions of rotor loads in hover OGE (Ref. 1), it is necessary to verify that that this timestep is suitable for side-by-side rotors IGE. In order to test the temporal convergence of IGE rotor simulations, side-by-side rotors at z/R = 1.0 with 3.0R hub-hub separation are simulated with timesteps corresponding to 1.0° and 0.5° of rotor rotation. Table 4 reports the mean integrated thrust and torque of both rotors averaged over 3 revolutions using each timestep.

Table 4: Loads generated using 1.0° and 0.5° timesteps

Time Step	Thrust	Torque
1.0°	648.7 N	60.84 N
0.5°	649.8 N	60.73 N
% difference	0.17	0.18

The predicted thrust and torque using 1° timesteps compares well to when finer 0.5° timesteps are used, with thrust and torque lying within 0.2%. Beyond rev-averaged loads, the unsteady forces generated by the rotor are also of interest. Fig. 30 plots the integrated thrust of the left rotor using both 1° and 0.5° timesteps. Naturally, some of the high-frequency content is lost when increasing from 0.5° to 1°, however most of the larger peaks in the loading history loads predicted at 0.5° are also captured at 1°. Not only do the peak-peak amplitudes compare well, but the phase of the signal is also similar between timestep levels. These results suggest that 1° timesteps provide a sufficient level of temporal convergence that they can capture the same load characteristics as those from a finer timestep.

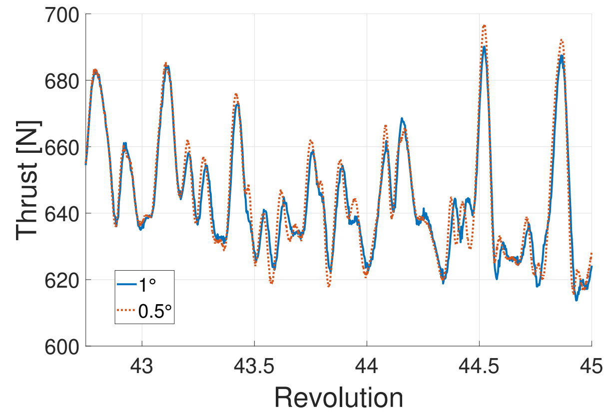

Figure 30: Left rotor instantaneous and rev-averaged thrust using 1° and 0.5° timesteps

Isolated Rotor IGE Validation

AcuSolve's® simulation of an isolated rotor IGE is compared to experiment presented in (Ref. 14). A 2-bladed rotor with 8° root pitch is chosen for comparison. This rotor is simulated at 900 RPM, both IGE at H/D = 1.0 and OGE. This differs somewhat from the setup described in (Ref. 14), where IGE rotors spun at 900 RPM are compared to an OGE rotor at 960 RPM. The simulation parameters, including blade mesh resolution are selected to be similar to those presented with Figs. (3 - 5). Integrated thrust values predicted by AcuSolve® are compared to experiment in Tab. 5, where experimental agreement IGE is found to lie within 1%.

In Tab. 5, the thrust predicted by AcuSolve® differs from experiment by 0.85%. AcuSolve® also predicts that T_{IGE}/T_{OGE} for this rotor is 1.02, which is consistent with that reported in (Ref. 15) and (Ref. 66), but slightly less than that reported in (Ref. 14) (1.05). Overall, the close agreement with experimental thrust and thrust increment suggests AcuSolve® is capable of accurately predicting ground effect phenomena.

ACKNOWLEDGMENTS

The authors would like to thank Rensselaer Polytechnic Institute and the Center for Computational Innovations. The findings from this study are made possible thanks to the availability of their computing resources and dedicated staff that maintain the network and hardware.

REFERENCES

1. Misiorowski, M., Gandhi, F., and Oberai, A. A., "Computational Study on Rotor Interactional Effects for a Quadcopter in Edgewise Flight," *AIAA Journal*, Vol. 57, (12), 2019, pp. 5309–5319. DOI: 10.2514/1.J058369

2. Misiorowski, M., Gandhi, F., and Anusonti-Inthra, P., "Computational Analysis of Rotor-Blown-Wing for Electric Rotorcraft Applications," *AIAA Journal*, Vol. 58, (7), 2020, pp. 2921–2932. DOI: 10.2514/1.J058851

Table 5: AcuSolve® validation of an isolated hovering IGE rotor at H/D = 1.0

H/D	AcuSolve Thrust [N]	Experimental Thrust [N]	% difference
1.0	33.37 (900 RPM)	33.66 (900 RPM)	0.85%
∞	32.64 (900 RPM)	33.657 (960 RPM)	-

3. Healy, R., Misiorowski, M., and Gandhi, F., "A CFD-Based Examination of Rotor-Rotor Separation Effects on Interactional Aerodynamics for eVTOL Aircraft," *Journal of the American Helicopter Society*, Vol. 67, (1), January 2022, pp. 1–12. DOI: 10.4050/jahs.67.012006

4. Healy, R., Gandhi, F., and Mistry, M., "Computational Investigation of Multirotor Interactional Aerodynamics with Hub Lateral and Longitudinal Canting," *AIAA Journal*, Vol. 60, (2), February 2022, pp. 872–882. DOI: 10.2514/1.j060530

5. Healy, R., McCauley, J., Gandhi, F., and Sahni, O., "A Computational Examination of Side-by-Side Rotors in Ground Effect," *Journal of the American Helicopter Society*, 2023. DOI: 10.4050/jahs.68.032007

6. Healy, R., and Gandhi, F., "Wing Lift Enhancement from Aft Rotor Induced Suction," Paper 1268, Vertical Flight Society 78th Annual Forum, Fort Worth, TX, May 2022.

7. Diaz, P. V., and Yoon, S., "High-Fidelity Computational Aerodynamics of Multi-Rotor Unmanned Aerial Vehicles," 2018 AIAA Aerospace Sciences Meeting, jan 2018. DOI: 10.2514/6.2018-1266

8. Yoon, S., Pulliam, T. H., and Chaderjian, N. M., "Simulations of XV-15 Rotor Flows in Hover Using OVERFLOW," AHS 5th Aeromechanics Specialists' Conference, San Francisco, CA, USA, Jan 2014.

9. Yoon, S., Lee, H. C., and Pulliam, T. H., "Computational Analysis of Multi-Rotor Flows," 54th AIAA Aerospace Sciences Meeting, January 2016. DOI: 10.2514/6.2016-0812

10. Yoon, S., Diaz, P. V., Boyd Jr., D. D., Chan, W. M., and Theodore, C. R., "Computational Aerodynamic Modeling of Small Quadcopter Vehicles," Proceedings of the 73rd Annual Forum, Fort Worth, TX, May 2017.

11. Miesner, S., Keßler, M., Krämer, E., and Schäferlein, U., "Investigation of Near Ground Effects in Hover Flight for the Multi-Rotor Aircraft Volocopter-2X," Proceedings of the 76th Annual Forum, October 2020.

12. Hebbar, U. U., Gandhi, F., and Sahni, O., "Parametric Investigation of Flow over a Rotor-Blown Wing using High-fidelity Simulations," Proceedings of the 78th Annual Forum, May 2022.

13. Fradenburgh, E. A., "The Helicopter and the Ground Effect Machine," *Journal of the American Helicopter Society*, Vol. 5, (4), October 1960, pp. 24–33. DOI: 10.4050/jahs.5.4.24

14. Hefner, R., and Knight, M., "Analysis of Ground Effect on the Lifting Airscrew," Technical Report 626, NACA TN, 1945.

15. Hayden, J. S., "The Effect of the Ground on Helicopter Hovering Power Required," Proceedings of the AHS 32nd Annual Forum, May 1976.

16. Light, J. S., "Tip Vortex Geometry of a Hovering Helicopter Rotor in Ground Effect," *Journal of the American Helicopter Society*, Vol. 38, (2), April 1993, pp. 34–42. DOI: 10.4050/jahs.38.34

17. Zbrozek, J., "Ground Effect on the Lifting Rotor," Technical Report 2347, Aeronautical Research Council, 1947.

18. Curtiss, H., Sun, M., Putman, W., and Hanker, E., "Rotor Aerodynamics in Ground Effect at Low Advance Ratios," *Journal of the American Helicopter Society*, Vol. 29, (1), 1984, pp. 48–55. DOI: 10.4050/jahs.29.48

19. Sheridan, P. F., and Wiesner, W., "Aerodynamics of Helicopter Flight near the Ground," Proceedings of the 33rd Annual AHS National Forum, Washington, DC, USA, May 1977.

20. Nathan, N. D., and Green, R. B., "The Flow Around a Model Helicopter Main Rotor in Ground Effect," *Experiments in Fluids*, Vol. 52, (1), October 2011, pp. 151–166. DOI: 10.1007/s00348-011-1212-1

21. Bhattacharyya, S., and Conlisk, A., "The Structure of the Rotor Wake in Ground Effect," 41st AIAA Aerospace Sciences Meeting and Exhibit, January 2003. DOI: 10.2514/6.2003-1255

22. Griffiths, D. A., Ananthan, S., and Leishman, J. G., "Predictions of Rotor Performance in Ground Effect Using a Free-Vortex Wake Model," *Journal of the American Helicopter Society*, Vol. 50, (4), October 2005, pp. 302–314. DOI: 10.4050/1.3092867

23. Moushegian, A. M., Smith, M. J., Whitehouse, G. R., and Wachspress, D. A., "Hover Performance in Ground Effect Prediction Using a Dual Solver Computational Methodology," Proceedings of the 77th Annual Forum, May 2021.

24. Whitehouse, G. R., Wachspress, D. A., and Quackenbush, T. R., “Aerodynamic design of helicopter rotors for reduced brownout,” International Powered Lift Conference Proceedings, Philadelphia, PA, 2010.

25. Saberi, H. A., and Maisel, M. D., “A Free-Wake Rotor Analysis Including Ground Effect,” , May 1987.

26. Graber, A., Rosen, A., and Seginer, A., “An Investigation of a Hovering Rotor in Ground Effect,” *The Aeronautical Journal*, Vol. 95, (945), 1991, pp. 161–169. DOI: 10.1017/S0001924000023812

27. Wadcock, A., Ewing, L., Solis, E., Potsdam, M., and Rajagopalan, G., “Rotorcraft Downwash Flow Field Study to Understand the Aerodynamics of Helicopter Brownout,” Proceedings of the AHS Southwest Region Technical Specialists’ Meeting, October 2008.

28. Kutz, B. M., Keßler, M., and Krämer, E., “Experimental and numerical examination of a helicopter hovering in ground effect,” *CEAS Aeronautical Journal*, Vol. 4, (4), jul 2013, pp. 397–408. DOI: 10.1007/s13272-013-0084-x

29. Brown, R. E., and Whitehouse, G. R., “Modelling Rotor Wakes in Ground Effect,” *Journal of the American Helicopter Society*, Vol. 49, (3), July 2004, pp. 238–249. DOI: 10.4050/jahs.49.238

30. Lakshminarayan, V. K., Kalra, T. S., and Baeder, J. D., “Detailed Computational Investigation of a Hovering Microscale Rotor in Ground Effect,” *AIAA Journal*, Vol. 51, (4), 2013, pp. 893–909. DOI: 10.2514/1.J051789

31. Tan, J. F., Sun, Y. M., and Barakos, G. N., “Vortex Approach for Downwash and Outwash of Tandem Rotors in Ground Effect,” *Journal of Aircraft*, Vol. 55, (6), November 2018, pp. 2491–2509. DOI: 10.2514/1.c034740

32. Ramasamy, M., and Yamauchi, G., “Using Model-Scale Tandem-Rotor Measurements in Ground Effect to Understand Full-Scale CH-47D Outwash,” *Journal of the American Helicopter Society*, Vol. 62, (1), January 2017, pp. 1–14. DOI: 10.4050/jahs.62.012004

33. Silva, M., and Riser, R., “CH-47D Tandem Rotor Outwash Survey,” American Helicopter Society 67th Annual Forum, 2011.

34. Potsdam, M., and Strawn, R., “CFD Simulations of Tiltrotor Configurations in Hover,” *Journal of the American Helicopter Society*, Vol. 50, (1), January 2005, pp. 82–94. DOI: 10.4050/1.3092845

35. Tran, S., Lim, J., Nunez, G., Wissink, A., and Bowen-Davies, G., “CFD Calculations of the XV-15 Tiltrotor During Transition,” Proceedings of the American Helicopter Society 75th Annual Forum, 2019.

36. Polak, D. R., Rehm, W., and George, A. R., “Effects of an Image Plane on the Tiltrotor Fountain Flow,” *Journal of the American Helicopter Society*, Vol. 45, (2), April 2000, pp. 90–96. DOI: 10.4050/jahs.45.90

37. Rajagopalan, R., “A Procedure for Rotor Performance, Flowfield and Interference - A Perspective,” 38th AIAA Aerospace Sciences Meeting and Exhibit, January 2000. DOI: 10.2514/6.2000-116

38. Gupta, V., and Baeder, J. D., “Quad Tiltrotor Aerodynamics in Ground Effect,” Proceedings of the 58th Annual AHS Forum, Montreal, Canada, June 2002.

39. Radhakrishnan Mylapore, A., and Schmitz, F. H., “An Experimental Investigation of Ground Effect on a Quad Tilt Rotor in Hover,” *Journal of the American Helicopter Society*, Vol. 60, (1), January 2015, pp. 1–14. DOI: 10.4050/jahs.60.012002

40. Radhakrishnan, A., and Schmitz, F., “An Experimental Investigation of a Quad Tilt Rotor in Ground Effect,” 21st AIAA Applied Aerodynamics Conference, June 2003. DOI: 10.2514/6.2003-3517

41. Radhakrishnan, A., and Schmitz, F., “Quad Tilt Rotor Aerodynamics in Ground Effect,” 23rd AIAA Applied Aerodynamics Conference, June 2005. DOI: 10.2514/6.2005-5218

42. Radhakrishnan, A., and Schmitz, F., “Aerodynamics and Lifting Performance of a Quad Tilt Rotor in Ground Effect,” Paper 292, Proceedings of the 63rd Annual Forum of the American Helicopter Society, Virginia Beach, VA, 2007.

43. Healy, R., McCauley, J., Gandhi, F., Sahni, O., and Mistry, M., “A Computational Investigation of Side-by-Side Rotors in Ground Effect,” Proceedings of the 77th Vertical Flight Society Annual Forum (Virtual), 2021.

44. Phillips, B., Hrishikeshavan, V., Yeo, D., and Chopra, I., “Experimental Evaluation of a Quadrotor Biplane with Variable Pitch Rotors,” 73rd Annual Forum of the American Helicopter Society, May 2017.

45. Aurora Flight Sciences, “PAV - Passenger Air Vehicle,” https://www.aurora.aero/pav-evtol-passenger-air-vehicle/, 2019.

46. Wisk, “Wisk Cora Aircraft,” https://wisk.aero/aircraft/, 2021.

47. Niemiec, R., and Gandhi, F., “Effect of Rotor Cant on Trim and Autonomous Flight Dynamics of a Quadcopter,” 74th Annual Forum of the American Helicopter Society, May 2018.

48. Niemiec, R., Gandhi, F., Lopez, M. J. S., and Tischler, M. B., “System Identification and Handling Qualities Predictions of an eVTOL Urban Air Mobility Aircraft Using Modern Flight Control Methods,” 76th Annual Forum of the Vertical Flight Society, October 2020.

49. Hosseini, Z., Ramirez-Serrano, A., and Martinuzzi, R. J., "Ground/Wall Effects on a Tilting Ducted Fan," *International Journal of Micro Air Vehicles*, Vol. 3, (3), sep 2011, pp. 119–141. DOI: 10.1260/1756-8293.3.3.119

50. Tritschler, J. K., Milluzzo, J. I., and Holder, J. M., "Performance Effects of Hover In-Ground-Effect over Sloped Terrain," Proceedings of the 75th Annual Forum, May 2019.

51. Publications, V. F. S., "Aurora PAV eVTOL model," https://gallery.vtol.org/search/images/?q=aurora+pav, June 2019.

52. Hariharan, N. S., Narducci, R. P., Reed, E., and Egolf, A., "AIAA Standardized Hover Simulation: Hover Performance Prediction Status and Outstanding Issues," 55th AIAA Aerospace Sciences Meeting, 2017. DOI: 10.2514/6.2017-1429

53. Abras, J., Narducci, R. P., and Hariharan, N. S., "Impact of High-fidelity Simulation Variations on Wake Breakdown of a Rotor in Hover," AIAA Scitech 2020 Forum. DOI: 10.2514/6.2020-0531

54. Niemiec, R., and Gandhi, F., "Development and Validation of the Rensselaer Multicopter Analysis Code (RMAC): A Physics-based Low-fidelity Modeling Tool," 75th Annual Forum of the Vertical FLight Society, Philadelphia, PA, 2019.

55. ACUSIM Software, I., "AcuSolve Validation - NACA 0012 Airfoil," Technical report, http://altairhyperworks.com/ResourceLibrary.aspx?category=Case2010, 2010.

56. Corson, D., Jaiman, R., and Shakib, F., "Industrial Application of RANS Modelling: Capabilities and Needs," *International Journal of Computational Fluid Dynamics*, Vol. 23, (4), 2009, pp. 337–347. DOI: 10.1080/10618560902776810

57. Altair Engineering Inc., *Modeling of Turbulence - Near-Wall Modeling*, acusolve/training_manual/near_wall_modeling_r, 2019.

58. Bazilevs, Y., Michler, C., Calo, V., and Hughes, T., "Weak Dirichlet Boundary Conditions for Wall-bounded Turbulent Flows," *Computer Methods in Applied Mechanics and Engineering*, Vol. 196, (49), 2007, pp. 4853 – 4862. DOI: https://doi.org/10.1016/j.cma.2007.06.026

59. Boisard, R., "Aerodynamic Investigation of a Helicopter Rotor Hovering in the Vicinity of a Building," Proceedings of the 74th Annual Forum, Phoenix, AZ, May 2018.

60. Duraisamy, K., and Baeder, J. D., "High Resolution Wake Capturing Methodology for Hovering Rotors," *Journal of the American Helicopter Society*, Vol. 52, (2), apr 2007, pp. 110–122. DOI: 10.4050/jahs.52.110

61. Richez, F., and Ortun, B., "Numerical Investigation of the Flow Separation on a Helicopter Rotor in Dynamic Stall Configuration," 42nd European Rotorcraft Forum, Lille, France, 11 2017.

62. Jansen, K. E., Whiting, C. H., and Hulbert, G. M., "A Generalized-α Method for Integrating the Filtered Navier–Stokes Equations With a Stabilized Finite Element Method," *Computer Methods in Applied Mechanics and Engineering*, Vol. 190, (3), 2000, pp. 305 – 319. DOI: https://doi.org/10.1016/S0045-7825(00)00203-6

63. N. Brooks, A., and J.R. Hughes, T., "Streamline Upwind/Petrov-Galerkin Formulations for Convection Dominated Flows with Particular Emphasis on the Encompressible Navier-Stokes Equations," *Computer Methods in Applied Mechanics and Engineering*, Vol. 32, (1-3), 09 1982, pp. 199–259. DOI: 10.1016/0045-7825(82)90071-8

64. Cheeseman, I., and Bennett, W., "The Effect of the Ground on a Helicopter Rotor in Forward Flight," Technical Report 3021, ARC R&M, September 1955.

65. Zhou, W., Ning, Z., Li, H., and Hu, H., "An Experimental Investigation on Rotor-to-Rotor Interactions of Small UAV Propellers," 35th AIAA Applied Aerodynamics Conference, June 2017. DOI: 10.2514/6.2017-3744

66. Fradenburgh, E. A., "Aerodynamic factors influencing overall hover performance," *Aerodynamics of Rotary Wings*, Vol. 7, (1), 1972.